Parameterizing Ion–Lipid Interactions from Local Clusters to Reproduce Bulk and
Interfacial Properties in Lipid Bilayers

by

Matthew W. Saunders

A thesis submitted in partial fufillment
of the requirements for the degree of
Doctorate of Philosophy in Biology
with a concentration in Cell & Molecular Biology
Department of Molecular Biosciences
College of Arts and Sciences
University of South Florida

Co-Major Professor: Sameer Varma, Ph.D.
Co-Major Professor: Sagar Pandit, Ph.D.
Jianjun Pan, Ph.D.
Libin Ye, Ph.D.
Stanley Stevens, Ph.D.

Date of Approval:
TBD

Keywords: Molecular Dynamics, ???

Contents

2

List of Tables

List of Figures

Abstract

1 Introduction[1]

1.1

2 A high dimensional parameter search method to determine force field mixing terms in molecular simulations[1]

Molecular dynamics (MD) force fields for lipids and ions are typically developed independently of one another. In simulations consisting of both lipids and ions, lipid-ion interaction energies are estimated using a predefined set of mixing rules for Lennard-Jones (LJ) interactions. This, however, does not guarantee their reliability. In fact, compared to the quantum mechanical reference data, Lorentz-Berthelot mixing rules substantially underestimate binding energies of Na^+ ions with small molecule analogues of lipid headgroups, yielding errors on the order of 80 and 130 kJ/mol, respectively for methyl acetate and diethyl phosphate. Previously, errors associated with mixing force fields have been reduced using approaches like 'NB-fix' in which LJ interactions are computed using explicit cross terms rather than those from mixing rules. Building on this idea, we derive explicit lipid-ion cross terms that also may implicitly include many-body cooperativity effects. Additionally, to account for interdependency between cross terms, we optimize all cross terms simultaneously by performing high-dimensional searches using our ParOpt software. The cross terms we obtain reduce the errors due to mixing rules to below 10 kJ/mol. MD simulation of lipid bilayer conducted using these optimized cross terms resolve the structural discrepancies between our previous simulations and small-angle X-ray and neutron scattering experiments. These results demonstrate that simulations of lipid bilayers with ions that are accurate up to structural data from scattering experiments can be performed without explicit polarization terms. However, it is worth noting that such NB-fix cross terms are not based on any physical principle; a polarizable lipid model would be more realistic, and is still desired. Our approach is generic and can be applied to improve accuracies of simulations employing mixed force

---

[1]FOOT!!

fields.

2.1 Introduction

Cellular membranes function as highly dynamic interfaces with many diverse components, including lipids, peptides, carbohydrates, and charged species like ionic salts. Studies of these complex systems often benefit from computational methods, particularly molecular dynamics (MD) simulations.[1] In our previous MD simulation studies, we characterized the effects of various monovalent and divalent ions on model 1-palmitoyl-2-oleoyl-sn-glycero-phosphatidylcholine (POPC) bilayers.[2–5] We reported that ions modify POPC bilayer structure with significant effects on area per lipid and bilayer thickness. Similar results were also reported in MD simulations by others.[6–10] Experiments characterizing bilayer structures in the presence of ions have not been as numerous as simulation studies. However, experimental findings indicate that dissolved salts at physiological concentrations do not modify bilayer structure significantly.[11–13] Specifically, Petrache *et al.* performed small angle X-ray scattering (SAXS) experiments on multilamellar vesicles of 1,2-dilauroyl-sn-glycero-3-sn-glycero-phosphatidylcholine as well as other lipids in KCl and BrCl salt solutions, and reported that while small changes can be seen in the X-ray scattering form-factor due to the salts, the fitted electron density profiles are essentially identical for systems with and without salt.[12] Similarly, Pabst *et al.* found no significant change in bilayer structure for POPC bilayers in NaCl salt at or below 1 M concentration.[11] Furthermore, Uhrikova *et al.* reported small structural changes using small angle neutron scattering (SANS) experiments on 1,2-dipalmitoyl-sn-glycero-3-sn-glycero-phosphatidylcholine vesicles interacting with $CaCl_2$.[13] Taken together, these results point to a general discrepancy between structural data from MD simulations and scattering experiments.

The reliability of MD simulations depends greatly on the force field (FF) parameters used for describing intra- and inter-molecular interactions. While FF parameters of lipids, including ours, are developed with great accuracy and care, we note that they are derived in the absence of ions. Similarly, ion parameters are also derived in the absence of lipids.[14]

3

When simulations of bilayers are conducted in salt solution, ion-lipid interactions are computed using FF mixing rules. In our previous MD simulations of POPC bilayers in salt solutions, we employed our gromos43A1-S3 lipid FF parameters[15] that were developed for use with SPC/E water to determine lipid-lipid and lipid-water interactions. Ion-ion and ion-water interactions were described using Joung and Chetham[14] parameters, also developed for use with SPC/E water. Lipid-ion interactions were estimated using Lorentz-Berthelot (LB) mixing rules for Lennard-Jones (LJ) components , and there was a significant change in bilayer structure compared to that of the bilayer without salt despite the relatively small initial salt concentration of 200 mM. Does this suggest that the discrepancy between our MD predictions and experiments is the result of the LB mixing rules? Note that none of the MD simulations of lipid-ion interactions discussed above include explicit terms to describe electronic polarization. Errors in mixing rules may, therefore, emerge if the high electric fields of ions induce cooperativity effects in lipid groups differently from those in water. Quantum mechanical (QM) studies, in fact, suggest that many-body cooperativty effects, such as polarization depend strongly on ion-coordinator chemistry.[16,17] It has also been postulated that these effects, and specifically electronic polarization may play an important role in determining the structure and dynamics of lipid bilayers – especially when interacting with ions.[18–22]

Small deviations from LB rules have been shown to have a significant effect on the behavior of systems of particles,[23] and it is possible that a systematic tuning of these parameters could be used to correct for artifacts in a simulation.[17,24–33] Such a 'Non-Bonded-fix' (NB-fix) strategy has been shown to effectively improve protein-ion , protein-nucleotide, and ion-membrane interactions while retaining the commonly used form of the LJ 6-12 potential .[17,24–33] Building on this idea, here we propose a more general approach to optimize interaction cross terms for use with the 6-12 potential, and also validate its prediction in condensed phase simulations. We expand on the NB-fix method by (a) optimizing all ion-lipid LJ cross terms simultaneously, and (b) implicitly including many-body cooperativity

4

effects. We consider simultaneous optimization of all cross terms to be critical, because of their strong, interdependent correlation with the target results.[34] This high-dimensional optimization is performed using our software tool ParOpt.[34,35] Many-body cooperativity effects have been shown to be a major contributor to ion binding[16] . Thus, it is important to include them in lipid bilayer simulations where ions are known to coordinate simultaneously with multiple ligands.[4]

We show that the cross terms we obtain from this approach substantially improve ion-lipid interaction energies over those obtained from LB mixing rules. MD simulation of a POPC bilayer in 200 mM NaCl initial solution conducted using these optimized cross terms also resolves the structural discrepancies between our previous MD simulations and small-angle X-ray and neutron scattering experiments at low salt concentrations.

2.2 Methods

The method proposed here is generic and can be applied to any pair of interacting species that use cross terms, and ensures that we are reproducing macroscopic results based on the most accurate representation of the local inter-molecular interactions. We chose small molecular analogues of the important ion binding sites in the polar region of phospholipid molecules. These molecules were also used as building block molecules in development of our lipid FF.[3,15] Specifically, we selected methyl–acetate (MeAc) to represent the ester group binding the acyl–chain to the glycerol backbone, and diethyl–phosphate (DePh) to represent the headgroup phosphate and surrounding carbons (See insert on figure ??). The overall goal was to take the substitution energy of ions from water to the selected molecules, along with the corresponding geometries, all computed using a benchmarked quantum mechanical framework, and optimize the interaction cross terms to reproduce these target data within the Molecular Mechanics force-field.

Combined analysis of results from experiments and *ab initio* molecular dynamics simulations in the aqueous phase suggest that Na^+ ions prefer to directly coordinate with $\sim 5-6$ water molecules .[36–40] However, when coordinating with MeAc molecules, steric hindrance

5

restricts the number of binding partners to fewer than four coordinating molecules. Thus, we limited the size of our MeAc clusters to up to four molecules around an ion. DePh has resonant oxygens on each molecule that potentially act as two binding sites, so we limited these clusters to up to two molecules around a Na^+. These were compared to the clusters of Na^+ surrounded by up to four water molecules. In this work, we forgo modifying terms for Cl^-, as we have found in our previous work that anions do not bind to the bilayer headgroup significantly, and remain solvated by water molecules.[3]

2.2.1 Quantum Mechanical Calculations

Target data for our parameter optimization consisted of energies and geometries computed using a benchmarked density functional theory as implemented in the FHI-Aims software package.[41] Geometry optimizations were performed on the $Na^+–(Water)_n$, $Na^+–(MeAc)_n, n \leq 4$, and $Na^+–(DePh)_m, m \leq 2$ clusters. These clusters were first optimized using the MM force field used in Kruczek *et al.* and Saunders *et al.*[3,5] MM optimized structures were then further optimized using the PBE0 functional[42,43] with self-consistent vdW corrections.[44] We used the *really tight* basis sets included in the FHI–aims software. This functional and basis set combination has been shown to perform well compared to experiment and high-level quantum methods for many different chemistries of ion-ligand clusters.[17,45,46] Optimizations were performed with a force maxima of 10^{-3} eV/Å , with total energies converged to within 10^{-6} eV. We computed substitution energies of these clusters as:

$$E_{\text{MeAc}}^n = E_{\text{Na}^+–(\text{MeAc})_n} - nE_{\text{MeAc}} - E_{\text{Na}^+–(\text{Water})_n} + nE_{\text{Water}}$$

$$E_{\text{DePh}}^n = E_{\text{Na}^+–(\text{DePh})_n} - nE_{\text{DePh}} - E_{\text{Na}^+–(\text{Water})_{2n}} + 2nE_{\text{Water}},$$

(2.1)

where n is the number of solvent molecules (see tables 2.1 and 2.2 for all of the QM data used for this computation). These substitution energies and corresponding configurations were used as targets for the parameter optimization.

Table 2.1: Total energies of systems of small molecules from QM calculations. These energies are computed by taking the total energy from the final step of geometry optimization on clusters of our selected small molecules around a single Na$^+$following the procedure outlined in the methods section. We computed binding energies using these values.

Cluster Size	Water (kJ/mol)	MeAc (kJ/mol)	DePh (kJ/mol)
1	-9.048×10^5	-1.130×10^6	-2.528×10^6
2	-1.609×10^6	-1.834×10^6	-4.630×10^6
3	-2.313×10^6	-2.538×10^6	N/A
4	-3.018×10^6	-3.243×10^6	N/A

Table 2.2: Self energies of isolated molecules. These are computed by performing geometry optimization on an isolated molecule following the procedure outlined in the methods.

	Water	Na$^+$	MeAc	DePh
Energy (kJ/mol)	-2.006E+05	-4.253E+05	-7.042E+05	-2.102E+06

2.2.2 Parameter Optimization

Parameter optimization is performed using our ParOpt software package .[34,35] This software is available for download at `https://csmlabfs1.cas.usf.edu/Sites`. We utilized the Nelder-Meade method to perform a search to simultaneously optimize all σ_{ij} and ϵ_{ij} cross terms of Na$^+$ ions with MeAc and DePh molecules. Specifically, there are seven atom types in these two small molecules (table 2.4), and so we optimized 14 cross terms for the 6-12 LJ potential. Error was determined by comparing the optimized geometries and substitution energies of each new parameter set to the reference data from QM.

Boundary constraints were imposed on ϵ_{ij} and σ_{ij} to keep the search space finite. Table S3 in supporting information shows all of the constraints placed on the parameter search. Additionally, we constrained the NA–OM σ_{ij} to be smaller than the σ_{ij} for NA–P to avoid unphysical conformations of DePh. Boundary constraints are enforced by reassigning σ_{ij} or ϵ_{ij} values that violate the bound to the boundary value. Throughout optimization we mon-

itored constraint violations and ensured that we did not select a final parameter set that is the result of a constraint violation. High–dimensional optimizations of this nature may not have a unique solution; thus, we performed 200 independent optimizations with random initial parameter values. We compared the parameter sets that best improved the substitution energy without significantly compromising the conformational geometries. Table 2.3 shows all constraints used in this parameter search.

Figure 2.1a illustrates a representative NM–trajectory that follows NM–error as a function of optimization step. In this case, the NM–error is defined as an equally–weighted combination of the mean absolute error of the substitution energy and the distances between each atom in the cluster and the Na^+ ion. Each NM–move used is illustrated as a point on the error curve (see Fogarty *et al.* for complete description of NM algorithm and moves[34]). The insert shows the root-mean squared distance (RMSD) between the simplex vertices at each step. As is typical with the NM method, error drops exponentially during the initial steps, and slows down towards the end of the optimization process. The termination condition for the optimization run is the collapse of the NM–simplex (defined by the RMSD $\leq 10^{-10}$). Figure 2.1b shows all of the 291,870 σ_{ij}-ϵ_{ij} pairs tested between Na^+ ions and the non–carbon atoms in the 200 independent optimization runs, and provides a visual perspective of the sampled parameter space. The parameter set that yielded the lowest error, as discussed in the results section, was chosen to perform MD simulations of a POPC bilayer.

Table 2.3: Nelder–Meade constraints. These values were used to constrain the parameter search space during the NM–optimization.

	NA-CH3		NA-CH2		NA-CO*		NA-OA,-OM*,-O*,-P		Additional Constraints
	Min	Max	Min	Max	Min	Max	Min	Max	N/A
σ_{ij}(nm)	0.2	0.5	0.2	0.5	0.2	0.5	0.2	0.5	$\sigma_{ij}^{\text{NA-OM*}} \leq \sigma_{ij}^{\text{NA-P}}$
ϵ_{ij}(kJ/mol)	0	0.79	0	0.81	0	0.83	0.05	7	N/A

(a)

(b)
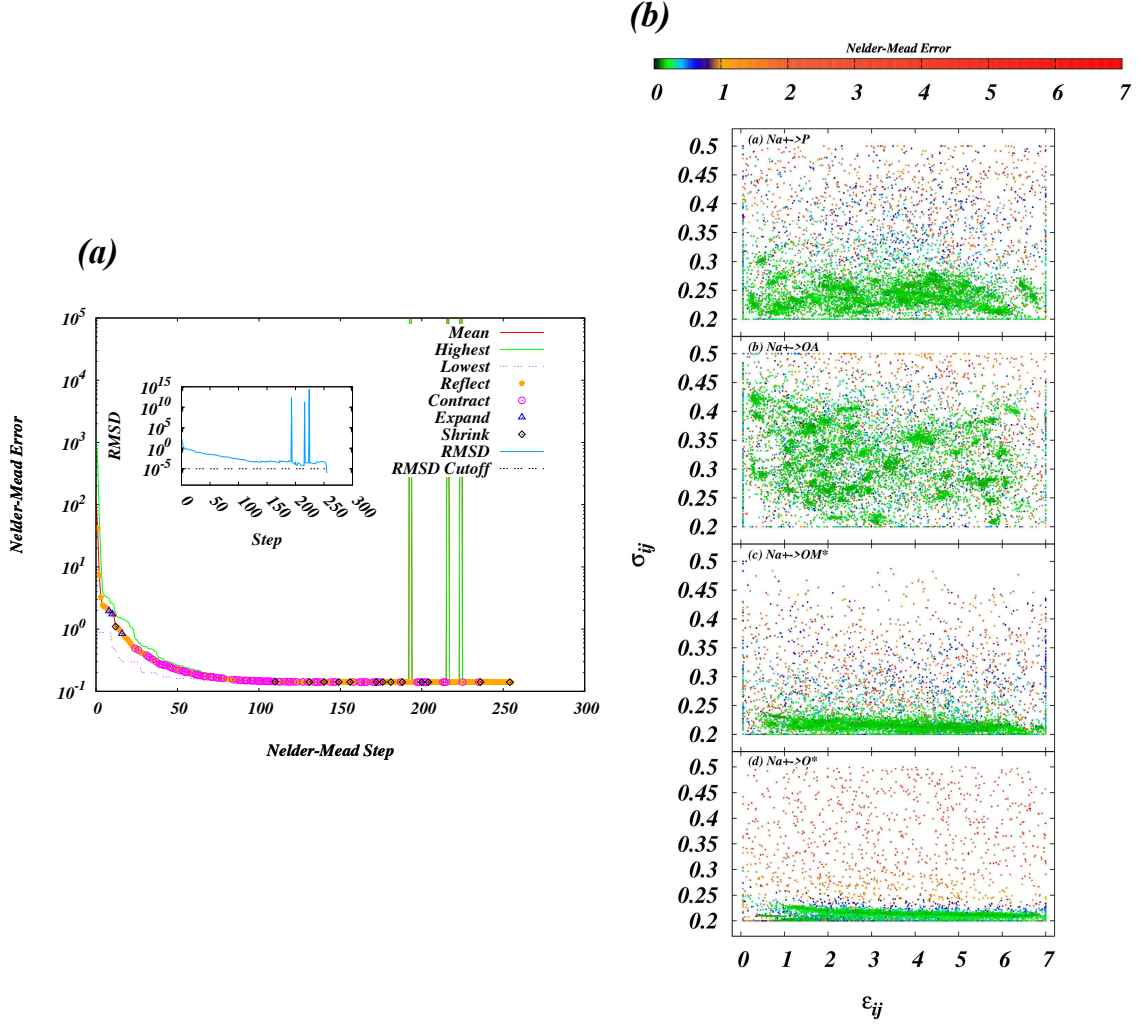
Figure 2.1: (a) Representative Nelder–Meade (NM) optimization run. Each point represents a move that the NM simplex can make while navigating the parameter space (See Fogarty *et al.* for a full description of the Nelder–Meade algorithm and available moves[34]). The insert illustrates the RMSD between the simplex vertices. The optimization is considered converged when the simplex collapses, which is defined by an RMSD $\leq 10^{-10}$. (b) Map of all σ_{ij} and ϵ_{ij} tested for interactions of Na^+ with non–carbon atom types in the 200 optimizations performed to find our final optimized set of cross terms. A total of 291,870 combinations of parameters were tested, shown color-coded according to their NM error.

2.2.3   Bilayer Construction

We first constructed a monolayer of POPC lipids by placing 100 lipids on a 10 nm by 10 nm grid, with excess space between the lipids to avoid overlaps in the lipid chains. Then we reflected this grid to create the second leaflet of the bilayer, resulting in a bilayer of 200 lipids.

Assuming a conservative estimate of one binding site per lipid, we need at least 200 Na^+ ions in bulk solvent at the beginning of the simulation to avoid complete depletion of bulk ions after equilibration. In order to do this we constructed a system with double the size of the solvent block used in our previous works.[3,4] This larger system was constructed by adding 60,000 waters to the system on a 3-D grid with excess space between waters, and randomly replacing water molecules with 216 Na^+ and 216 Cl⁻. This results in an initial concentration of 200 mM, similar to our previous simulations. This process resulted in a simulation box with dimensions 9.75 nm × 9.75 nm × 59.84 nm.

We energy-minimized the simulation box using the steepest descent algorithm with a force tolerance of 50 kJ $mol^{-1}nm^{-1}$. Neighbor searching was performed every 2 steps. The PME algorithm was used for electrostatic interactions with a cut-off of 1.6 nm. A reciprocal grid with a spacing of 0.12 nm^{-1} was used with 6th order B–spline interpolation. A single cut-off of 1.6 nm was used for van der Waals interactions.

We then performed a 200 ps constant pressure simulation at 290 K to ensure the system was relaxed enough for further annealing. The box dimensions at the end of this were 7.86 nm × 7.86 nm × 32.90 nm. Annealing was started at 400 K, and the system was cooled to the production simulation temperature of 300 K in steps of 10 K. Each step was simulated for 150 ps, giving a total annealing time of 1.5 ns. The annealing process shrunk the box dimensions to 7.97 nm × 7.97 nm × 32.14 nm. This final structure was used as the starting point for production run.

2.2.4 Molecular dynamics

All molecular dynamics simulations were performed with the GROMACS software package, version 5.1.6.[47–51] We have utilized the SPC/E model for all waters.[52] Lipid interaction terms are described using the parameters in the gromos43A1-S3 parameter set developed by our group in previous work.[15] The system temperature was held constant at the production run temperature of 300K using the Nosè–Hoover thermostat with a coupling constant of 0.5 ps.[53] Pressure coupling was performed using the Parrinello-Rahman semiisotropic barostat, which held the system pressure constant at 1 atm with a coupling constant of 1.5 ps.[54] The P–LINCS algorithm was used to constrain all bonds in the system to allow for a 4 fs integration timestep.[55] Integration was carried out using the Verlet scheme, with neighborlist updates taken on every other integration step. We used a cutoff of 16 Åfor short–range electrostatics. Beyond this cutoff, we have used the smooth particle–mesh Ewald summation method to describe electrostatics.[56] LJ interactions were calculated with a cutoff of 16 Å. For all systems described, we have simulated continuously for 0.7 μs.

Simulated trajectories were analyzed using a combination of GROMACS built–in analysis tools and in–house software developed on the GROMACS API.

2.3 Results and Discussion

2.3.1 Optimized Cross-Terms

The final optimized parameters are detailed in table 2.4 alongside the original parameters computed using LB rules. We immediately note a general trend of an increase in the value of ϵ_{ij} for the non-carbon atom types. With our constraints on the carbon atoms, we have nudged the optimization into gaining the binding energy by increasing the ϵ_{ij} for the specifically electronegative atoms. Values of σ_{ij} have changed, but remained close to the original values in general, suggesting that the optimum distance to the minimum energy of the LJ potential is estimated well by LB rules. We can also see that no values of σ_{ij} or ϵ_{ij} violate the constraints described in table S3 in supporting information. We examined

11

Table 2.4: Force–field cross terms. Original terms, as used in the system simulated with LB rules were computed by applying Lorentz-Berthelot mixing rules to the LJ parameters of Na$^+$and each lipid component atom type. Optimized parameters are the result of the NM–optimization using ParOpt.[34,35] All constraints on the search space can be seen in figure S3 in supporting information.

	Original		Optimized	
	σ_{ij}(nm)	ϵ_{ij}(kJ/mol)	σ_{ij}(nm)	ϵ_{ij}(kJ/mol)
NA-CH3	0.295	1.100	0.235	0.700
NA-CH2	0.312	0.772	0.237	0.809
NA-OA	0.256	1.120	0.211	3.035
NA-P	0.277	1.900	0.301	0.483
NA-OM*	0.252	1.221	0.211	1.445
NA-CO*	0.335	0.362	0.315	0.758
NA-O*	0.251	1.221	0.216	2.440

substitution energies and corresponding conformational geometries by running energy min-imization of the QM–optimized structures using the final parameter set. These were then analyzed using the GROMACS built–in energy and distance tools. The substitution energies and the conformations for this parameter set are shown in figure 2.2 and in figure 2.3, re-spectively. We can see that for MeAc we have substantially improved substitution energies relative to those obtained from using LB mixing rules, which started with an discrepancy of around 30–80 kJ/mol. We have also improved the relative substitution between the clusters of various sizes. The substitution energies for DePh have also improved by a similar mag-nitude. The conformational geometries are largely unchanged, with a general trend of the binding distance to OM shrinking on the order of 0.25 Å in DePh. This shrinkage is common when optimizing both energies and conformations with the relatively small number of free parameters corresponding to the LJ cross terms.[17]

We also note that the substitution energies for both molecule types improve more in the larger cluster sizes. Larger clusters are more relevant to the dense environment in the lipid headgroup region of the bilayer, as few, if any, ions bind to a single lipid at a time.[3]
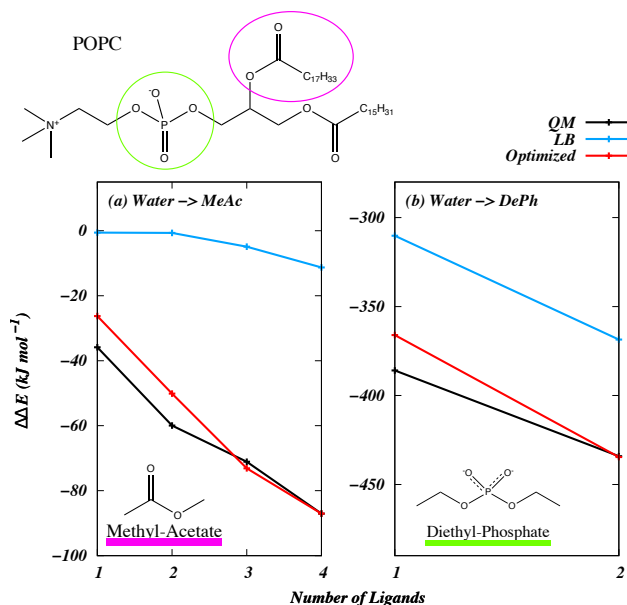
Figure 2.2: Substitution energies for Na^+ clusters computed as described in equation 2.1. In black we see the energies of systems computed using the standard mixing rules, in red we have the energies from benchmarked DFT, and in blue the optimized results. We see a significant error with the standard LB mixing rules, which is substantially improved with our new optimized cross terms. The insert shows an diagram of POPC, and the small molecules Methyl-Acetate (MeAc) and Diethyl-Phosphate (DePh) that were used to represent the major Na^+ interaction sites on the POPC molecule.

Furthermore, the substitution energy profile for MeAc has become much closer to that of the QM profile. Thus, these new parameters substantially improve the energetic balance between the lipid–ion, lipid–water and ion–water interactions.

The conformational geometries were mostly unchanged with the new parameter set, as even the original parameters do a good job in reproducing the QM–configurations. The least precise cluster appears to be for 4 MeAc, where the original LB parameters poorly represent the symmetries exhibited in the QM data. Even with the improvement from our new parameters, we may be missing behavior from explicit polarization effects that cannot be captured properly by a non–polarizable model.[16]
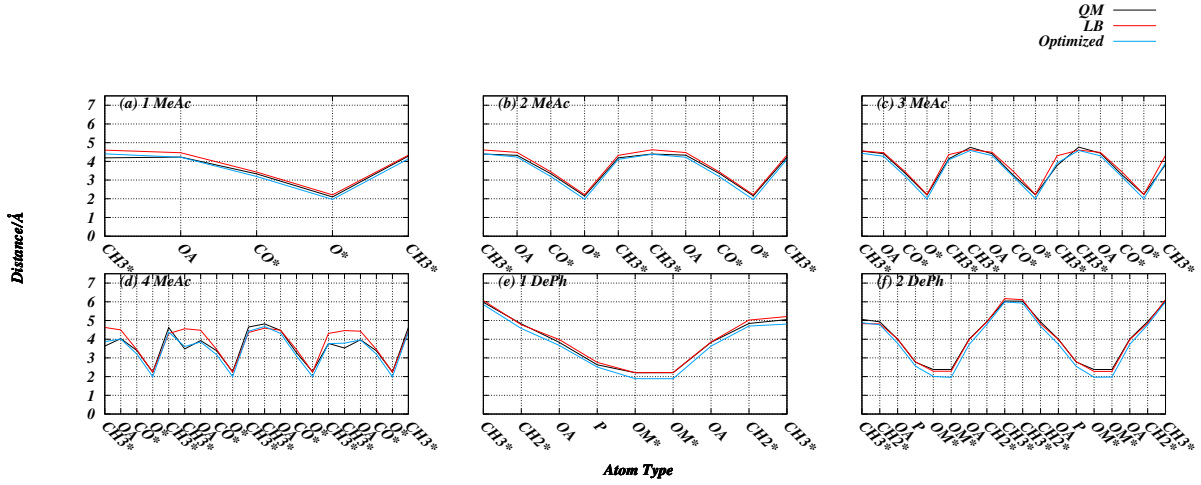
13

Figure 2.3: Distances from Na$^+$ to each component atom in sample clusters. We compute the geometry of our sample clusters by computing the distance from the ion to each other atom in the system, shown per atom type. These distances are used in combination with the substitution energies in figure 2 to compute the error for the NM optimization.

2.3.2 Validation of Parameters

In order to characterize our new parameter set in a bilayer, we generated a 700 ns simulation of a bilayer of POPC lipids in NaCl salt solution, and we compared the results against a similar system that we simulated using LB rules in our previous works.[3,4] These older trajectories for systems both with salt and without will be referred to, respectively, as LB and 'without salt.' We simulated our system with optimized cross terms, hence forth will be referred to as the 'optimized' system, long enough to equilibrate the number of bound ions (see figure 2.6). We will further characterize this ion binding in a subsequent section.

Bilayer Structure

Bilayer structural parameters can be seen in table 2.5. The phospholipid component volumes V_H and V_C (lines 1 and 2) are computed following the procedure outlined by Petrache *et al.*[57] The lipid chains are identified as starting at the first carbon attached to the lipid

Table 2.5: Bilayer structural parameters. D_{hh} is the peak–to–peak distance from the electron density of the lipid bilayer, and is a measure of bilayer thickness. Bilayer thickness D_B and chain thickness $2D_C$ are computed from number densities of the solvent and the lipid chains, respectively. V_H, and V_C are the volumes of the headgroup and lipid chains computed using the method from Petrache *et al.*[57] V_L is the sum of V_H and V_C. Rows 7-11 contain kinetic parameters for ion binding to membrane. These parameters come from fitting the equation $N_b(t) = \frac{K_a}{K_a + K_d} N \left(1 - \exp\left[-\left(K_a + K_d\right)\left(t - t_0\right)\right]\right)$ to the data for the number of ions bound to the lipid bilayer across the simulation time. A is the asymptotic number of ions bound to the lipid bilayer, and can be used as the expected number of ions that will bind to the system at equilibrium. τ is the characteristic timescale of the fitted function. n_0 is the number of ions bound at the beginning of the production run of the simulation. K_D and K_A are the computed binding association and dissociation constants, and K_A/K_D is the binding rate constant.

	Without salt	LB	Optimized
D_{HH} (Å)	37.44 ± 1.07	40.18 ± 1.04	37.64 ± 0.88
D_B (Å)	36.54 ± 0.47	40.90 ± 0.31	39.36 ± 0.43
$2D_C$ (Å)	27.07 ± 0.34	30.33 ± 0.29	28.97 ± 0.34
V_H (Å^3)	310.68 ± 1.14	316.13 ± 0.83	314.81 ± 0.75
V_C (Å^3)	904.89 ± 1.28	891.79 ± 1.65	896.50 ± 1.19
V_L (Å^3)	1215.57 ± 1.00	1207.92 ± 1.57	1211.32 ± 1.21
K_A (ns^{-1})	N/A	$7.12 \times 10^{-3} \pm 8.18 \times 10^{-5}$	$2.65 \times 10^{-3} \pm 1.74 \times 10^{-5}$
K_D (ns^{-1})	N/A	$3.20 \times 10^{-3} \pm 4.75 \times 10^{-5}$	$3.58 \times 10^{-3} \pm 2.83 \times 10^{-5}$
A	N/A	74.51	91.88
τ (ns)	N/A	96.73	160.54
K_A/K_D	N/A	2.225	0.74

chain carbonyl oxygen, including the oxygen. The atom groups not part of the lipid chains are partitioned into the headgroup volume. We take the number–density of these component groups along with that of the solvent, and use them to optimize the objective function:

$$\Omega(v_i) = \sum_{z_j}^{\rho_s} (1 - \sum_{i=1}^{N_{\text{Groups}}} (\rho_i(z_j)v_i)^2), \tag{2.2}$$

In the equation above, $\rho_i(z_j)$ is the number density of the i component in the z_j slice of the box and v_i is the corresponding component volume. The component volumes are then multiplied by the corresponding number of particles per molecule per group – 32 for the chain particles, and 20 for the headgroup. This gives us the total volume per molecule for each group. The total lipid volume V_L (line 3 in table 2.5) is taken to be the sum of these two values. These remain relatively similar in all three systems, as this value is intrinsic to the lipid molecule and should not change with the inclusion of ions.

Structural data are obtained for lipid bilayers via small angle X-ray and neutron scattering experiments as a one–dimensional form–factor. Data are then fitted to a continuous function to retrieve number and electron densities for the various lipid components.[58,59] Our simulations allow us direct access to the electron densities and number densities. The entries in table 2.5 are determined from these densities.

Figure 2.4 shows the electron densities and corresponding bilayer form-factors. Form–factors are computed by taking the cosine–transform of the symmetrized electron densities. We note that the simulations carried out using LB rules produced a thicker bilayer and had different details at the peak region of the density. The new parameter set results in similar electron density to that of the system without salt. This is similar to the results reported by Petrache *et al.* and Pabst *et al.*, where for systems with less than 1 M NaCl, the differences in the electron densities were not discernible.[11,12] These electron densities are used directly to measure the value of D_{hh}, defined as the peak–to–peak distance (see table 2.5 line 4). The new parameter set corresponds to a smaller D_{hh}, similar to the system without salt.
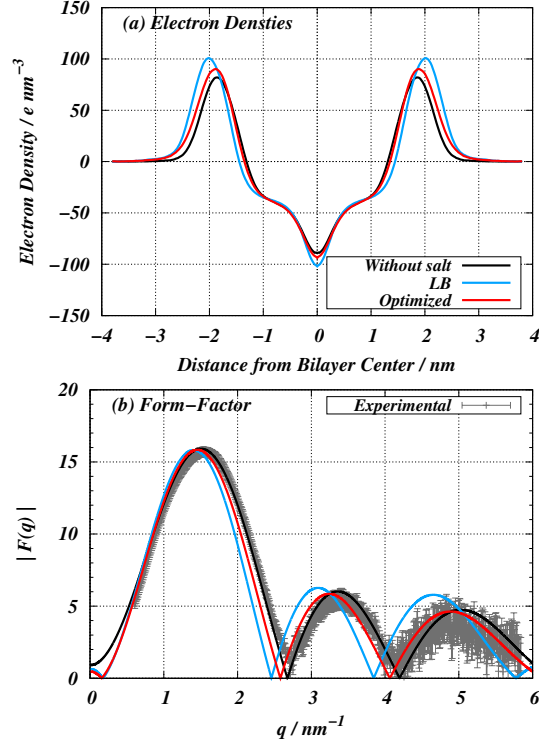
Figure 2.4: Electron densities of the simulated bilayers (a), and corresponding bilayer form–factors (b). Electron densities as obtained using the GROMACS density tool, centered at the minimum to define the bilayer center, and with the electron density of solvent subtracted. The simulated with optimized parameters appears to lack the large peak seen in the system simulated with LB rules, and appears more similar to the bilayer structure of a bilayer simulated without salt. This is further reflected in the bilayer form–factor, computed by taking the cosine–transform of electron density. Experimental SAXS results are for a POPC bilayer in pure solvent.[59] We see the first lobe of the optimized system moves closer to the experimental results and the form–factor of a system without salt. This lines up with experimental results, that have shown small, if any, change in the bilayer SAXS form–factor.[11–13]

In addition to D_{hh}, different measures are used to assess the bilayer thickness that relies on the probability densities of different components of the system. It can be shown that D_B (see table 2.5 line 5) computed by integrating one minus the probability density of solvent and ions is equivalent to the computation of the Luzzati thickness of the total bilayer.[15,59] We define probability of finding a particular component in a slice of the box as,

$$P_i(z) = \frac{\rho_i(z)}{\sum_j^n \rho_j(z)},$$
(2.3)

17

where $\rho_i(z)$ are the number densities for the component particles (i) of the system as a function of the z-position of each slice of the box, and the summation ranges over all components in the particular slice. Thus,

$$\mathrm{D_B} = \int_{\text{Box length}} \left(1 - P_{\text{water+ions}}(z)\right) dz. \qquad (2.4)$$

In table 2.5 line 2, the $\mathrm{D_B}$ is larger for the systems with ions, but the value obtained using our new parameter set is closer to that of the bilayer simulated without salt.

We use a similar definition of probability density for $2\mathrm{D_C}$, computed from the probability distribution of the lipid chains. This component is defined by the hydrocarbon chains starting after the ester–linkage on both the Sn1 and Sn2 terminal of the lipid backbone. This value (line 6 in table 2.5) is increased in the system simulated with LB rules over the system without salt, as we reported in our previous work. However, the new parameter set yields a value similar to the system without salt, which is consistent with the smaller overall thickness of the bilayer simulated with optimized cross terms.

The differences in bilayer thickness are closely related to the packing of the lipid chains in the hydrophobic core of the bilayer. When the chains become more disordered, the bilayer thickness typically drops.[58] Lipid chain ordering can be determined experimentally by performing NMR on specifically deuterated hydrocarbon chains. Since we lack hydrogen on our coarse–grained lipid chains, we cannot directly access the C–D ordering. Instead, we compute the chain order tensor $S_{\alpha\beta}$ defined as

$$S_{\alpha\beta} = \frac{1}{2}\langle 3\cos\theta_\alpha \cdot \cos\theta_\beta - \delta_{\alpha\beta}\rangle,$$

where the angles θ_α and θ_β are the angles between the molecular axis and the box z-direction. We then use this tensor to calculate the S_{CD} as

$$-S_{CD}^{\text{Saturated}} = \frac{2}{3}S_{xx} + \frac{1}{3}S_{yy} \qquad (2.5)$$

for saturated carbons,[60] and as

$$-S_{CD}^{\text{Unsaturated}} = \frac{1}{4}S_{zz} + \frac{3}{4}S_{yy} \mp \frac{\sqrt{3}}{2}S_{yz} \qquad (2.6)$$

for unsaturated carbons.[61] These values are plotted per each carbon in the lipid chain in figure 2.5 in supporting information. As reported in our previous simulations, the addition
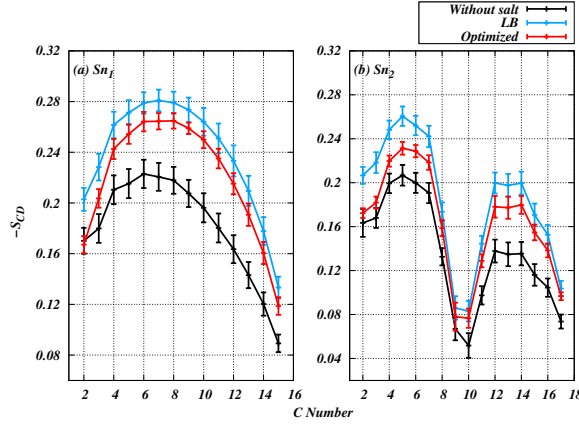

Figure 2.5: Lipid chain deuterium order parameters. S_{CD}s are computed for each carbon for the chains Sn1 (a) and Sn2 (b), starting at the second carbon in the chain. We see that the optmized system is still showing significant ordering in the lipid chains as a result of ion binding; however, the ordering is less pronounced than in the system simulated with LB rules, and is closer to that of the simulation without salt. This result corresponds with the smaller bilayer thickness in the optimized system.

of salt has an ordering effect on the lipid chains. This effect is also seen in our new parameter set; however, the ordering is less pronounced, which is consistent with the notion that the bilayer structure is not significantly altered at physiological salt concentration.[11,12]

While this result indicates a structure more consistent with experimental results, the detailed structure of a lipid bilayer is a result of the delicate balance between ion–lipid, lipid–water, and ion–water interactions. In order to fully understand how our new parameter set has altered the overall bilayer structure, we next characterize the specific interactions between these moieties.

2.3.3 Membrane-Salt Interactions

Both ions and solvent compete for the binding sites on the lipid headgroup. As seen in figure **??**, the new cross terms produce a relatively stronger interaction between $Na^+$and lipid headgroup components compared to that of the LB rules. Thus, there is potentially a reduction in the available binding sites for the solvent. To examine how the new cross terms have altered ion interactions with lipids in the bilayer, we first characterize the dynamics of ion binding to the lipid bilayer.

We define ion binding to the lipid bilayer when half or fewer of its first shell coordinators are not waters. In order to compute the equilibrium binding constant, we must determine the equilibrium number of bound ions to the lipid surface. Figure 2.6 shows the number of bound ions as a function of time over the entire duration of the simulation. We note that
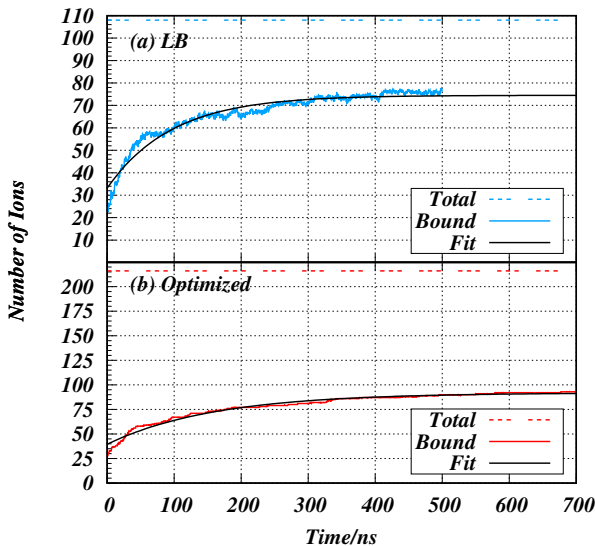
Figure 2.6: Number of ions bound to the lipid bilayer as a function of simulation time. The exponential fits to this data are also shown. These fits are used to compute the asymptotic number of ions bound as well as binding rate constants. 'Total' refers to the total number of ions in each simulation box. A membrane bound ion is defined as having half or fewer of its first coordination shell occupied by water molecules.

even after 700 ns of simulation time, the number of bound ions are not fully equilibrated. Thus, we use first–order reaction kinetics to estimate the asymptotic number of bound ions.

20

The first–order reaction kinetics are modeled as a differential equation:

$$\frac{dN_b}{dt} = K_a \left(N - N_b \right) - K_d N_b,$$

(2.7)

where N_b are the number of bound ions, and K_a, K_d are the association and dissociation time constants, respectively. The solution of this differential equation is:

$$N_b(t) = \frac{K_a}{K_a + K_d} N \left(1 - \exp\left[- \left(K_a + K_d \right) \left(t - t_0 \right) \right] \right).$$

(2.8)

This solution is fit to the data in figure 2.6, and the resulting fit is also plotted. The fitting parameters are listed in table 2.5. The first–order reaction kinetic model fits reasonably well to the data from both the systems, except in the beginning of the simulation where the effect of the annealing process is more pronounced; however, we are only interested in the asymptotic behavior of the fit as this is representative of the equilibrium state of the system. The asymptotic number of bound ions as $t \to \infty$, $A = \frac{K_a}{K_a + K_d} N$ (table 2.5 row 9), is larger in the system simulated with optimized terms. We also report the timescale of ion binding $\tau = \frac{1}{(K_a + K_d)}$ for both systems (table 2.5 row 10). The timescale of binding in the system using optimized cross terms is longer, and suggests that this system would need more time to equilibrate than the system simulated with LB rules. Finally, we report the value of $\frac{K_a}{K_d}$ (table 2.5 row 11), which we observe is much smaller with the new parameter set than compared to that of the system simulated with LB rules.

To examine how specific interactions between ions and lipids are modified by the new parameters, we tracked the binding partners of ions across the box over the last 150 ns of simulation time. Moieties are considered to be bound to an ion if they are within a distance of 3.3 Å from the Na^+ ion. Several electronegative groups in the simulation can potentially bind to the Na^+ ion. We compute the number of these potential binding partners within the first shell of each Na^+ ion across the simulation box. Ions are then sorted according to their box z-positions, and then the data are averaged over the last 150 ns. This is plotted in

21

figure 2.7. We note first that the total number of solvating oxygens of ions within the bilayer
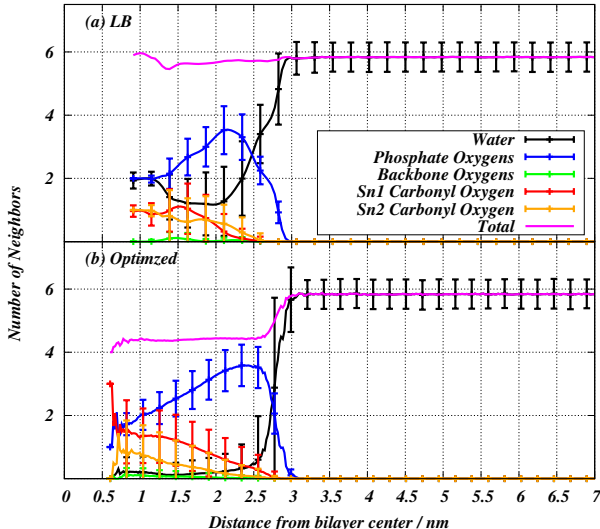

Figure 2.7: Chemistry of Na^+ inner shell coordination as a function of distance from bilayer center. Compared to the system simulated with LB rules (a), the system simulated with optimized cross terms (b) yields a lower Na^+ total coordination number within the headgroup region of the bilayer. This drop in coordination appears to be due to a greater dehydration of the ions in this system.

headgroup region with the optimized parameter set has dropped by ~ 1 when compared to ions in similar locations in the system simulated using LB rules. This is not surprising, given the dependence of ion coordination preferences on the local environment.[62] The binding to other lipid oxygens has not been altered much by the new parameter set; however, we do note that water within the headgroup region does not appear to be strongly associated with ions.

2.3.4   Water Structure and Dynamics

To further characterize the dehydration of ions in the new simulated system, we look to the lipid– and ion–water interactions. Figure 2.8 shows the number density of water as a function of distance from the bilayer center for each of our simulated systems, with the $2D_C$ and D_B illustrated as dotted lines. We see that our new parameter set produces a
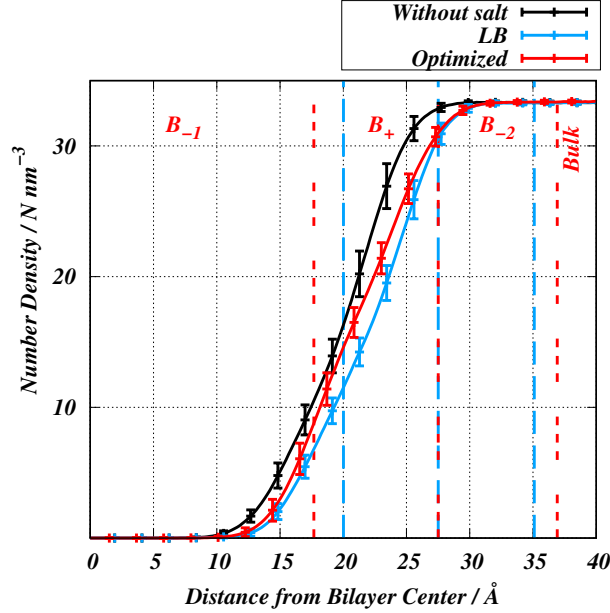
Figure 2.8: Water density at the bilayer interface. We illustrate the regions regions B_{-1}, B_+, B_{-2} and $Bulk$ for each system with dotted lines. We see that the optimized cross terms yield a greater density of solvent in the B_+ and B_{-1} regions over the system simulated with LB rules. We also see the density in these regions of the system optimized with optimized cross terms is more similar to that of the system without salt.

bilayer interface that has more solvent inside the headgroup region, between $10 - 25$ Å from the bilayer center. This density is more similar to that of the system simulated without salt. This suggests that the dehydration of ions in the system simulated with optimized parameters does not correspond to a dehydration of the lipid bilayer.

Next, we characterize the orientational structure of the water. Figure 2.9 examines the water order parameter across the simulation box. We identify perturbed water structure by examining first (P_1) and second (P_2) orientational order parameters for the OW→HW1 bond of water with respect to the z-axis of the simulation box (β). These order parameters are defined using the first and second Legendre polynomials with respect to the angle β,

$$
\begin{aligned}
P_1 &= \langle \cos(\beta) \rangle \\
P_2 &= \frac{1}{2} \left\langle \left(3\cos^2(\beta) - 2 \right) \right\rangle,
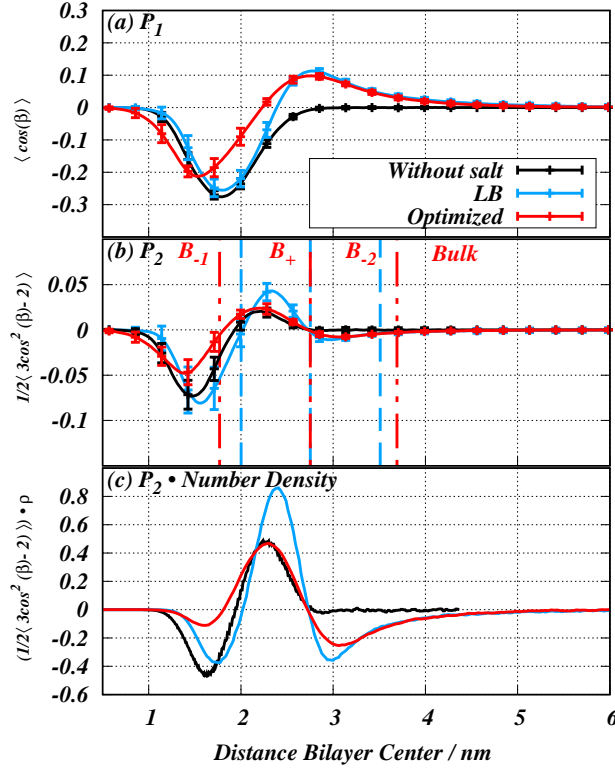\end{aligned}
\tag{2.9}
$$

23

Figure 2.9: Water orientational order parameters P_1 (a) and P_2 (b), and the product of the water number density and P_2 (c). We see in P_1 and P_2 less ordering in the waters in the optimized system, suggesting that waters may be less strongly interacting with ions or lipid components. We denote the four regions of the lipid bilayer based on the shape of the P_2 data as dotted lines in (b).[5] We have not included these regions for the system without salt, as the P_2 data does not include the same details as the systems with salt. The integral of (c) is related to the quadrupolar splitting constant $\Delta\nu$ found in deuterium NMR experiments. This also gives a closer look at how solvent is ordered in the headgroup while accounting for the amount of solvent in the region. We see that optimized cross terms result in a significant drop in the area under the curve, which is much closer to the shape of the data from the system without salt. The regions B_{-2} and $Bulk$ are not within the bilayer headgroup, and are expected to be less affected by the new parameter set.

where average is over all the waters in a particular volume slice of the box and then over simulation time. We plot these values as a function of distance from the bilayer center. P_1 denotes dipolar ordering of the bond vector and the bilayer normal direction, with a positive value indicating an average outward orientation and a zero value corresponding to an average perpendicular orientation to the bilayer normal or a uniformly random orientation. We observe a similar pattern of ordering across the box in all systems; however, we see an

24

overall reduction in ordering with our new parameter set when compared to both the LB and the no–salt system. We also see the inner minimum of the order parameter moved further into the bilayer when compared to LB, which is consistent with the larger quantity of water in this region that we observe in the water densities.

Following the protocol established in our previous work,[5] we identify three regions within the bilayer interface, B_{-1}, B_{+}, B_{-2}. The B_{-1} region is defined as the region of negative ordering starting at the bilayer center, and ending when the order parameter values cross zero at the start of the B_{+} region. The B_{+} region starts at the end of the B_{-1} region, and is the area of positive ordering, ending where the order parameter crosses zero again. The B_{-2} region starts at the end of the B_{+}, and extends out to where the second order parameter goes to zero. This was found by fitting an exponential function to this region and taking the scale parameter from that fit as the boundary with bulk solvent. We find that water is significantly less perturbed by the bilayer with our new parameter set. We have also computed $P_2 \cdot \rho_{\text{Water}}$, shown in shown in figure 2.9(c). This value relates the amount of water in each region of the box and the overall ordering in the region. We still see significantly less ordering with the new parameter set, and even with the larger number of waters in the bilayer headgroup. The integral of this curve is related to the quadrupole splitting $\Delta\nu$ observed in in deuterium NMR experiments.[3,63]

This suggests that while there is more solvent in the interface, it is perhaps not associated with either Na^{+}or lipids, and may remain less structured than in the system simulated with LB rules. This can be further ascertained by the diffusion coefficients of waters in each of the regions defined by P_2. We compute the mean square displacement (MSD) for water oxygens in each region by first tracking which waters remain in the region. Any waters that leave the region are removed from the MSD calculation. We chose a duration of 100 ps to track the MSD in order to have a sufficiently long time for the MSD to become linear, while still maintaining a statistically significant number of waters in the slice. A line is fit to the middle 80% of the MSD, and the fitted slope is used to calculate the diffusion coefficient following

Einstiein's relation for 2D diffusion

$$\lim_{t \to \infty} \frac{\left\langle (r(t) - r(0))^2 \right\rangle}{(t - t_0)} = 6D. \tag{2.10}$$

These values can be seen in table 2.6. We note that the water in the headgroup region,

Table 2.6: Diffusion coefficients of water in different regions of the lipid bilayer, defined by the shape of the second orientational order parameter of water molecules in the box. These regions are defined by the shape of the distribution of the second orientational order parameter across the simulation box. B_{-1} is the region of negative ordering starting at the bilayer center, and ending when the order parameter values cross zero. B_+ starts at the end of the B_{-1}, and is the region of positive ordering ending where the order parameter becomes negative. This starts the B_{-2} of negative ordering, extending out to where the second order parameter goes to zero, where we have *Bulk* solvent. We see that the optimized parameters result in slightly increased diffusion in the solvent, which correlates with the reduced ordering of the water dipoles and quadrupoles in the system.

	LB ($\times 10^{-10} m^2/s$)	Optimized ($\times 10^{-10} m^2/s$)
B_{-1}	1.11 ± 1.10	1.88 ± 2.41
B_+	4.23 ± 1.14	6.11 ± 2.83
B_{-2}	18.11 ± 4.23	21.29 ± 4.12
Bulk	27.32 ± 1.15	27.25 ± 1.36

corresponding to B_{-1} and B_+, diffuses slightly faster with the new parameter set, indicating more mobile water in these regions. However, the computed diffusion coefficients are within the error bars that of the system simulated with LB rules. Diffusion in the B_{-2} and *Bulk* regions are similar in both systems, as these are mostly outside of the bilayer and should not be affected by the new parameter set.

2.3.5   Bilayer Electrostatics

We further characterize the electrostatic properties of our bilayer systems by computing the electrostatic potential across the simulation box. We do this following the protocol used in Saunders *et al.*[5] We first compute the charge density of the system components. We integrate this distribution twice, setting both constants of integration to be zero to enforce

a zero value for the electric field in bulk solvent and a zero electrostatic potential at the box edge. This is accomplished by taking the average value of the electric field in the *bulk* region of the box defined earlier, and subtracting this value from all points. Due to the larger system size in the optimized system, we needed to compute the average value of a much larger region than in LB in order to apply boundary conditions. We then integrate again to get the electrostatic potential. This result can be seen in figure **??** in supporting information. The shape of the potential is largely unaltered within fluctuations. Systems simulated with
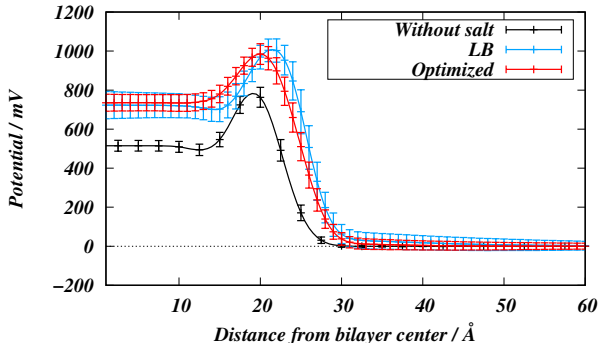

Figure 2.10: Electrostatic potential as a function of distance from bilayer center. The optimized cross terms yield a small change in the location of the peak of the potential in the bilayer simulated with optimized cross terms, as well as the loss of the valley behind the peak.

the optimized parameters and with LB rules both have a similar bilayer dipole potential, which remains elevated over the system without salt, by ~ 220 mV. We report that the optimized system has a slightly elevated bilayer dipole potential compared to the system simulated with LB rules, increased by ~ 12 mV. This may be a direct result of the larger number of ions bound to the bilayer in this system. We also note the system simulated with optimized cross terms has different details throughout the electrostatic potential compared to the system simulated with LB rules and in the system without salt, however these are within fluctuations and cannot be used to draw conclusions.

Poisson–Boltzmann (PB) theory is a mean field approximation for solvated ions near an interface. Experimentally PB theory is used to assess the surface potential of the lipid bilayers. We also examine the behavior of the ions in bulk solvent under the framework of

27

PB theory. Following the procedure used in our previous work,[5] we fit the number density of Cl⁻ions in the solvent–occupied region of the box to a Poisson-Boltzmann distribution, using the inverse Debye length K and the density of Cl⁻at the center of the solvent occupied region of the box ρ_0 as fit parameters. The density is modeled as:

$$\rho(z) = \rho_0 \exp\left(-\bar{z}e\beta\psi(z)\right), \tag{2.11}$$

where ρ_0 is the number density of the ion at the center of the solvent–occupied region of the box, $\bar{z} = 1$ is the valency of the ion in the system, $\beta = \frac{1}{k_b T}$, e is the charge on an electron, and $\psi(z)$ is the electrostatic potential. We then assume the form of $\psi(z)$ to be the sum of two Debye-Huckel potentials[64] reflected across the center of the solvent–occupied region of the box:

$$\begin{aligned}
\psi_1(z) &= \psi_s \exp(-K(z + \frac{D}{2})) \\
\psi_2(z) &= \psi_s \exp(K(z + \frac{D}{2})) \\
\psi(z) &= \psi_1 + \psi_2,
\end{aligned} \tag{2.12}$$

where D is the distance from the hydration boundary of one bilayer leaflet to the next across the solvent, K is the inverse Debye length, and ψ_s is the surface potential:

$$\psi_s = \frac{\varsigma}{\varepsilon_0 \varepsilon K}. \tag{2.13}$$

The LB system yielded a value of $D = 13.167$ nm and the system simulated with optimized parameters, containing twice as many solvent molecules, gave a value of $D = 27.01$ nm. We take the surface charge density ς from the charge density inside of the hydration boundary of the lipid bilayer. Since only ions contribute a net charge to our system, we compute this using only the charge density of ions in the system. This value was computed to be $\varsigma = 0.13\ e\ \text{nm}^{-2}$ for the system simulated with LB rules, and $\varsigma = 0.11\ e\ \text{nm}^{-2}$ for the

28

system simulated with the new parameters. Our fitting procedure yielded number densities $\rho_0 = 0.043\text{nm}^{-3}$ for the system simulated with LB rules, and $\rho_0 = 0.079\text{nm}^{-3}$ for the system simulated with optimized parameters. The fitted inverse screening lengths were found to be $K = 0.91 \pm 0.014$ nm^{-1} for the LB rules simulation and 0.94 ± 0.018 nm^{-1} for the system simulated with optimized parameters. The resulting fit and predicted density of Na$^+$ions and electrostatic potential can be seen in figure 2.11 in supporting information. We see the
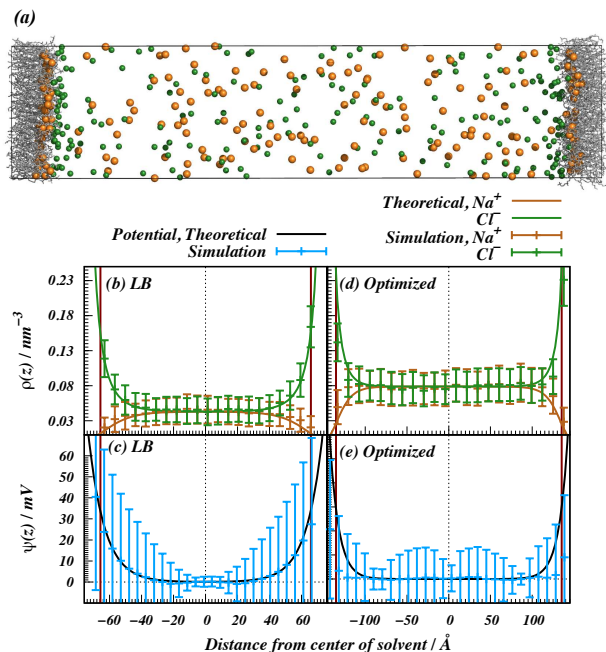

Figure 2.11: Poisson-Boltzmann theory predictions and simulation results. (a) shows a snapshot of the system simulated with optimized cross terms, translated to center the solvent occupied region. Water has been hidden for clarity. (b) and (d) show the number density of ions in the solvent occupied region of the box. (c) and (e) show the corresponding electrostatic potential in solvent. We illustrate theoretical predictions as solid lines, with corresponding simulation results as points with error bars. Red vertical lines denote the *hydration boundary* of the lipid bilayer. Cl$^-$density data is used for fitting in both systems.

results from our simulation represented by points with error bars, while PB theory results are shown in solid lines. We see excellent agreement in the Na$^+$density profile away from the bilayer surface, and reasonable agreement in the electrostatic potential. From this we can see that the optimized and LB systems both exhibit similar ionic distributions with models used to describe electrophoretic mobility experiments.[64]

2.4 Conclusions

Mixing rules are often relied upon to compute non–bonded cross terms for interacting molecules in molecular simulations. However, when mixing force–fields that have been developed independently of each other, inaccuracies may develop. Here we demonstrate one such case and propose a rigorous solution. MD simulations conducted using predefined mixing rules for non-polarizable force fields developed separately for ions and lipids have always produced very pronounced salt-induced structural changes in lipid bilayers. Contrary to this, most experimental observations point to a moderate or even an insignificant change in bilayer structure at physiological salt concentrations. We resolve this discrepancy by explicitly parameterizing ion–lipid cross terms using our procedure *"Many Body Non Bonded fix"* (MB-NB-fix). It is based on the NB-fix method employed in previous works [24–32] and utilizes ParOpt software developed in our lab[34].[35] We note that after applying the optimized parameters for Na^+–lipid interactions, the bilayer structure conforms more to experimental observations while all other properties such as solvent structure, electrostatic potential, and dynamic properties are approximately similar to that obtained with those obtained with LB parameters. We note that we have not applied this method to optimize Cl^- interactions terms, which may still further affect the bilayer structure. This will be the subject of future work.

The MB-NB-fix method proposed here is a general method which can be used to derive mixing terms for simulations with independently developed force fields. This method will be used in future work to improve other sets of mixed force-fields, including those of other monovalent ions and the gromos 43A1-S3 lipids, and between these lipids and amino-acids for use in proteins. Furthermore, many body cooperativity effects, such as ion-induced polarization in lipid molecules may be critical to further improving the reproduction of lipid bilayer structure. A correct approach to incorporate these effects to our simulation would be to have explicit polarization terms in our simulation models. This is complicated, as most existing polarizable simulation models are either not very effective at accurately reproducing

polarization effects or are much more computationally expensive compared to classical non-polarizable simulations. The MB-NB-fix method has potential to become an ideal solution for mixing force-fields, including polarizable and non-polarizable models in the same system to construct simulations that are tractable yet accurate.

3 Adsorption modes of Na^+, Li^+, and Mg^{2+} to a model zwitterionic lipid bilayer

The adsorption of ions to soft-porous interfaces plays a critical role in many physical and biological processes, such as the function of electrochemical energy storage devices or the attachment of membrane proteins to cells surfaces. In this work we characterize different adsorption modes, and describe the adsorption behavior of Na^+, Li^+, and Mg^{2+} onto a porous substrate. We identify three categories of adsorption based on the degree of dehydration of the ion, viz., steric adsorption corresponding to a lack of dehydration, imperfect adsorption with partial dehydration, and perfect adsorption representing total dehydration. Using 1-palmitoyl-2-oleoyl-sn-glycero-3-phosphatidylcholine (POPC) in salt solution as a generic model system for salt at a soft and porous interface, based on the simulation model used we find that anions, Cl^-, always adsorb sterically. Among cations, the divalent Mg^{2+} does not dehydrate, and is also adsorbed sterically. On the other hand, Na^+ adsorbed to a large fraction perfectly and Li^+ exhibits a significant fraction of imperfectly adsorbed ions, We demonstrate that, with everything else held fixed, the adsorption mode of a cation is determined solely by the strength of the electric field produced by the ion at the distance of the hydration shell.

3.1 Introduction

Interactions of ions with soft, porous, and charge-neutral substrates such as zwitterionic lipid bilayers are important and a common system of interest in soft matter physics and biophysics. Empirical studies towards these use simplified models to interpret observations, e.g. assuming the water as a dielectric continuum, or taking the ions as a spherical entity surrounded by a neatly organized hydration shell.[64]

A simple way of defining adsorption of ions to a substrate comes from the Poission-

Boltzmann (PB) theory.[64] This mean-field approximation predicts accumulation of ions near a surface due to the mutual electrostatic repulsion of the ions and entropic factors. Deviations in ion distribution from the predictions of PB theory near a substrate are the defining characteristic of the specific adsorption phenomenon .[65,66]

Experimental studies of ion adsorption can be broadly classified into two main groups – methods that examine the electric field/surface potential produced by the adsorbed ions, e.g, electrophoretic mobility[67] or measurement of the forces between bilayers,[68] and methods that can more directly characterize the location and dynamics of ions such as x-ray or neutron scattering,[13,37,58,59,69,70] and NMR.[28,58,71]

At the atomistic level, identifying adsorbed ions poses a different kind of challenge. We have addressed this issue previously, where we characterized adsorption by examining the dehydration of ions near the interface.[3,4,72,73] This is similar to the kind of adsorption described by the Langmuir isotherm model, where it is assumed that ions stick to a soft, porous interface through direct interaction.[74] Adsorption defined thusly has been reported in our previous works for monovalent ions such as Na^+ and Li^+.[3–5,75] Further, our previous work on divalent ions exhibited that Mg^{2+} maintains its hydration structure regardless of where the ion is located in the lipid bilayer,[4] yet maintaining a distribution distinct from that predicted by PB theory. Hence, in this work we characterize different modes of adsorption corresponding to different ions. Here we categorize the adsorption behavior based on degree of dehydration, starting from no dehydration at all as in the case of Mg^{2+} and Cl^-, extending to complete dehydration as in the case with Na^+. In the somewhat different context of RNA, which is not a soft, porous substrate, the specific binding of ions has been addressed extensively [76–80] based on the mobility of cations and further characterized by models that describe the structure of their coordination shell. Cations bound to RNA are frequently distinguished as being diffuse (similar to our steric adsorbed case), and the site-bound ions are further characterized by outer-shell (again analogous to our steric adsorption ions) or inner shell binding (analogous to the imperfect or perfect adsorbed ions), depending on the

folded conformation of the RNA or nearby nucleotides.[76–80]

Along with dehydration, we use specific adsorption in the context of PB density as the defining property of adsorption phenomenon. Based on our previous as well as current atomistic simulations we broadly classify adsorption of ions into three categories – viz. *perfect adsorption, imperfect adsorption*, and *steric adsorption*. We also demonstrate that, using different force-field for Mg^{2+} the predominant mode of adsorption of Mg^{2+} to 1-palmitoyl-2-oleoyl-sn-glycero-3-phosphatidylcholine (POPC) is always *steric adsorption*.

3.2 Methods

We perform multiple simulations of POPC bilayers with LiCl and $MgCl_2$ salt. Configurations for each simulation are listed in table 3.1. Bilayers are constructed of 200 lipids, with 100 lipids per leaflet. Simulations are all performed with 60,000 water molecules to ensure that the simulation box was large enough to have no long-range dipole moment, and have a significant sampling of bulk water. The inclusion of ions substantially increases the region of ordered waters in the system.[4,75] We simulate these systems with a starting concentration of 200 mM salt, in order to ensure that the equilibrium bulk concentration is physiologically relevant and yet statistically viable. Systems with Mg^{2+} are simulated with twice the number of anions to counter the +2 charge of the cation. All the systems are simulated for 1 μs of simulated time. The Mg^{2+}–Li *et al.*system is extended to 2.5 μs to confirm the long residence time of waters in the first coordination shell of Mg^{2+}.[83] It is observed that ions in the bilayer still do not exchange of waters from their first coordination shell, so another 1 μs simulation is performed using the water-Mg^{2+} interaction model developed by Grotz *et al.*, which significantly increase the water-exchange rate to be closer to the value observed experimentally.[83] All the simulations are performed using the GROMACS molecular dynamics software package, version 5.1.6,[47–51] and analysis is performed using GROMACS built–in analysis tools and in–house software developed on the gromacs API or using the MDanalysis python package.[84–86]

Table 3.1: Simulation system details. Each simulated system is started with 200 mM salt, and the final bulk concentration is computed from the average number density of ions at the center of the solvent occupied region of the box, from the last 150 ns of simulation time. Na^+–Saunders *et al.*simulation trajectories are published in our previous work, and are re-analyzed in this work. The Mg^{2+}–Li *et al.*system is extended to 2.5 μs to ascertain if any exchange of waters from the first shell of Mg^{2+}could be observed. Li^+(a) parameters are obtained from the work by Joung and Chetatham III.[14] Mg^{2+}(b-c) parameters are obtained from Li *et al.*[81] and Grotz *et al.*,[82] respectively.

System	No. of Cations	No. of Anions	Starting Bulk Salt Concentration	Final Bulk Salt Concentration	Simulated Time
Na^+From Saunders *et al.*2022[75]	216	216	200mM	103mM	0.7μs
Li^+(a)	216	216	200mM	102.0mM	1μs
Mg^{2+}(b)	216	432	200mM	152mM	2.5μs
Mg^{2+}(c)	216	432	200mM	153mM	1μs

3.2.1   Bilayer Construction

Lipid bilayers in solvent are constructed by placing POPC lipids on a 10 x 10 grid, and reflecting to create the second bilayer leaflet. 60,000 solvent molecules are then placed into the box above the bilayer grid, with random solvent molecules replaced to add ions (see table **??** for numbers of ions and types in each system). Systems are energy minimized using the steepest-descents algorithm to remove bad-contacts. Following energy-minimization, both systems are allowed to settle in an NPT dynamic run at a temperature of 250K for 1 ns. Systems are then annealed by heating to 350K, and cooling in steps of 10K to the simulation run temperature of 300K in steps of 155 ps. The final annealed configurations for each system are used as the initial configuration for the production molecular dynamics simulations.

3.2.2   Molecular dynamics

For total length of simulation runs, see table **??**. All systems are simulated with a time step of 4 fs. Neighbor searching is performed every 2 steps. The PME algorithm is used for electrostatic interactions.[56] with a cut-off of 1.6 nm. A reciprocal grid of $56 \times 56 \times 224$ cells is used with 4th order B-spline interpolation. A single cut-off of 1.6 nm is used for Van der Waals interactions. Temperature coupling is imposed with the Nose-Hoover algorithm.[53]

Pressure coupling is imposed with the Parrinello-Rahman algorithm.[54]

3.2.3 Force-field parameters

Lipid-lipid and lipid-water interactions are described using our gromos43a1-s3 model,[15] which is calibrated to work with the SPC/E water model.[52] Li^+-water interactions are described using Joung and Cheatham parameters.[14] We use the method described in Saunders *et al.*2022[75] to compute non-aqueous cross-terms for Li^+(see supporting table S1,and figures S1 and S2 for details). <mark>TODO</mark> PUT THOSE HERE Development of models describing the interactions of $Mg^{2+}$with water remains an elusive problem, and there are numerous models developed to describe Mg^{2+}–water interaction with varied levels of complexity.[81,82,87,88] These models are optimized to improve the hydration free energies as well as binding energies with various solvent models.[81,82,87] Previous work by our group has examined Mg^{2+}models from Li *et al.*and Allner *et al.*[81,87] in simulations with POPC lipids,[4] and found little variation among them in terms of their effects on lipid bilayer properties. With this in mind, we chose to focus our work here on the parameters developed by Li *et al.*because their optimization procedures closely follow our focus on binding energies. In recent work it has been reported that the existing Mg^{2+}parameters, including those developed by Li *et al.*overestimate the residence time for a water molecule in the first coordination shell of an ion.[82] In our past works using this force-field we reported insignificant Langmuir type adsorption of Mg^{2+}ions to the POPC bilayer, with waters retained in the first coordination shell of the ion.[4] We have also performed simulations with the parameters developed by Grotz *et al.*that directly reduce residence times while not significantly changing other solvation properties of the ion.[82,83] This was done to study how the interactions with water could affect the first-shell coordination of Mg^{2+}in the bilayer interface. We have computed the interaction cross-term for the Mg^{2+}ion from Grotz *et al.*with SPC/E water explicitly, using the Lorentz-Berthelot mixing rules.

3.3 Results and Discussion

3.3.1 Bilayer simulations of Li$^+$and Mg^{2+}

Lipid bilayer structure

The distribution of electron dense and heavy atoms is often studied by using scattering techniques, like small-angle x-ray and neutron scattering. These methods yield a scattering form-factor. Densities can be obtained from the form-factor by solving the inverse problem, which is a technically hard problem. In experiments this is usually solved by fitting a model to the form-factor. Simulations give us direct access to atomic positions, and consequently the densities. This allows us to compute a scattering form-factor by taking a cosine transform of the density. The computed form-factor can be compared with the direct measurements of the experiment. The simulated lipid bilayer x-ray scattering form-factors and associated electron densities for each system are shown in figure 3.1. We compare all form-factors for
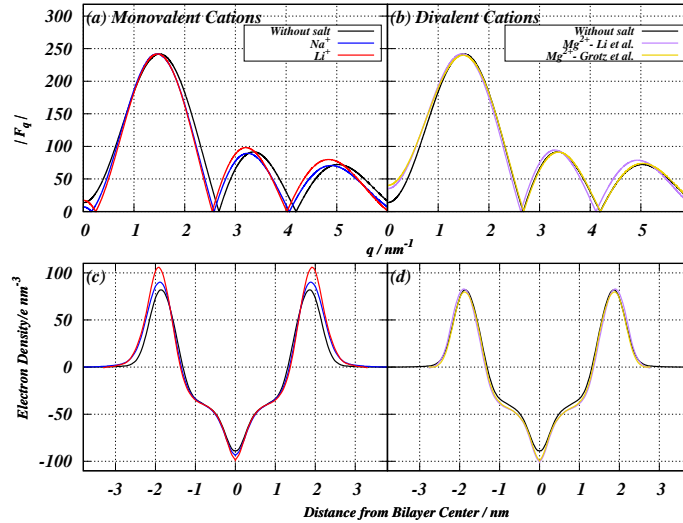

Figure 3.1: Comparison of x-ray scattering formfactors (a,b) and associated electron densities (c,d) for simulated systems. The system with Li$^+$salt has a slightly thicker bilayer compared to Na$^+$and the simulation without salt (a,c) and, Mg^{2+}does not significantly change the bilayer thickness under any parameter set studied (b,d).

each system to that of a system simulated without salt, published in our previous work.[3]

The bilayer thickness D_{hh} is determined by measuring the distance between the peaks in the

electron density, which roughly localize the electron-dense phosphates in the lipid headgroup – the values for this can be seen in table 3.2.

Experiments often report various types of thicknesses, volumes, and cross-sectional areas that are model dependent. We also compute these quantities to compare the simulation results with experiments. These values are presented in table 2.5. Based on the D_{hh} and the $2D_C$ there is a slight thickening of the bilayer in the Li^+ simulation above that seen in the Na^+ simulation. The Mg^{2+} simulations , irrespective of the parameter set, yield much less thickening than the Li^+ simulation. The volumes per lipid (V_L), headgroup (V_H), and chains (V_C) are computed using the method of Petrache $et\ al.$[57] This is done by optimizing the function:

$$\Omega(v_i) = \sum_{z_j}^{\rho_s} (1 - \sum_{i=1}^{N_{\text{Groups}}} (\rho_i(z_j)v_i)^2), \tag{3.1}$$

where $\rho_i(z_j)$ is the number density of the i component in the z_j slice of the box and v_i is the corresponding partial component volume. N_{Groups} is the number of atom groups for which we are dividing the system volume into component volumes – we have groups for solvent plus ions, lipid chain without the terminal methyls (CH_*), terminal methyls (CH_3), and the lipid headgroups (H). The lipid volumes are then computed as

$$V_C = N_{CH_*} \times v_{CH_*} + N_{CH_3} \times v_{CH_3} \tag{3.2}$$

and

$$V_H = N_H \times v_{\text{headgroup}}, \tag{3.3}$$

where $N_{CH_*} = 30$, $N_{CH_3} = 2$, $N_H = 20$ are the number of united atoms per atom group for CH_*, CH_3, and H. The chain volume V_C is similar for all systems studied, and there is some variation in the headgroup volume V_H . However, this method of dividing up the volume is more prone to errors in the headgroup region due to significant overlap between the headgroup and solvent densities. Thus, we also see similar variation in the total lipid volume

Table 3.2: Bilayer simulation details, and structural parameters. Here we detail the various structural measurements of each simulated bilayer. D_{hh} is the distance measured between the peaks in the electron density, which localize the electron-dense phosphate moiety in the lipid headgroup. D_B is a distance between the Gibb's surfaces[59] on the probability density of solvent as it approaches the lipid bilayer. $2D_C$ is the distance between the Gibb's surfaces on the probability density of lipid chains, and represents the lipid chain thickness. Volume per lipid V_L is measured by dividing the volume of the entire system into solvent and ions, and lipid following the method by Petrache $et\ al.$[57]. This V_L is the sum of the V_H and V_C, which are the volume per lipid headgroup and volume per lipid chains respectively. Area per lipid molecule A_L is computed as the ratio of twice the lipid chain volume V_C with $2D_C$. We also report the position of the hydration boundary of each system, which we compute as the point where the second water order parameter $P_2(cos(\beta)) \approx 0$ as was done in Saunders $et\ al.$2019[5].

	No Salt	Na$^+$	Li$^+$	Mg^{2+}–Li $et\ al.$	Mg^{2+}–Grotz $et\ al.$
D_{hh}(nm)	3.744 ± 0.107	3.764 ± 0.088	3.864 ± 0.070	3.832 ± 0.364	3.768 ± 0.525
D_B(nm)	3.654 ± 0.047	3.936 ± 0.043	4.511 ± 0.048	4.325 ± 0.044	4.213 ± 0.049
$2D_C$(nm)	2.707 ± 0.034	2.897 ± 0.034	3.015 ± 0.034	2.880 ± 0.029	2.809 ± 0.032
V_L($\times 10^{-3}$nm^3)	1215.57 ± 1.0	1211.32 ± 1.21	1201.2 ± 1.05	1219.8 ± 1.24	1227.7 ± 1.24
V_H($\times 10^{-3}$nm^3)	310.68 ± 1.14	314.81 ± 0.75	306.0 ± 1.01	324.0 ± 1.26	327.9 ± 1.10
V_C($\times 10^{-3}$nm^3)	904.89 ± 1.28	896.50 ± 1.19	895.3 ± 0.91	895.8 ± 1.05	899.8 ± 1.06
A_L($\times 10^{-2}$nm^2)	66.86 ± 0.85	61.89 ± 0.73	59.39 ± 0.69	62.21 ± 0.63	64.35 ± 0.82
Hydration Boundary (nm)	2.79	3.69	3.63	3.48	3.33

V_L. The two-dimensional area per lipid A_L is defined as $\frac{2V_c}{2D_c}$ as is often reported from SAXS and SANS experiments,[58] and is an important measure of how the lipids condense as the bilayer thickens. Both the simulations with Mg^{2+}yield bilayers with a larger A_L than the monovalent ions studied in this work, and are closer in area to the simulation without salt.

The detailed structure of molecules and their neighborhoods are often studied using various nuclear magnetic resonance (NMR) techniques. At present, these experiments with various salts are sparse. Thus, we report these data with anticipation that future experiments will fill this gap and validate or invalidate these numbers. Lipid chain ordering is determined via the acyl chain S_{CD} per carbon atom. These can be seen in figure 3.2.

There is significant increase in chain ordering in the systems with Na$^+$and Li$^+$, which is consistent with the slight thickening of the bilayer seen in the D_B values. The less coordinated Mg^{2+}systems have remained much closer to the ordering seen in the no-salt simulation.
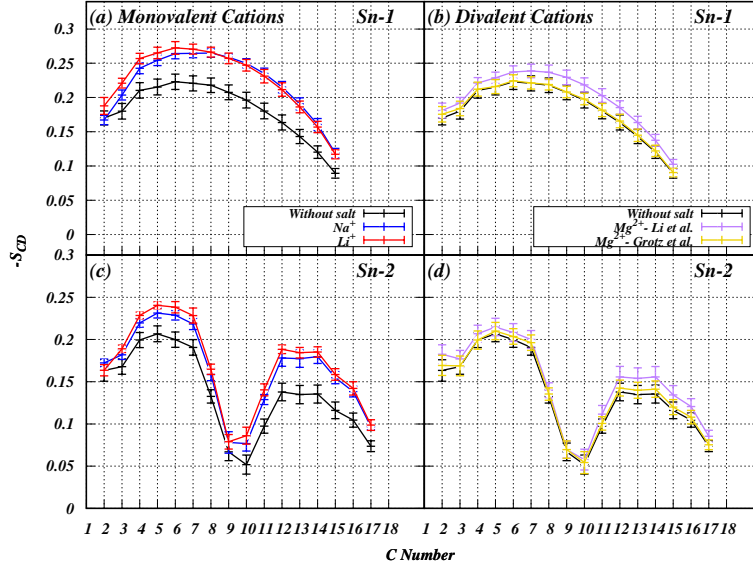
Figure 3.2: Acyl chain carbon-deuterium order parameters. These are computed for the Sn1 and Sn2 chains of each lipid starting at the second carbon in the chain.[60,61] We note that the lipids simulated in systems of monovalent ions (a,c) show a significant increase in the lipid chain ordering for both acyl chains. The systems simulated with Mg^{2+}(b,d) are much closer in ordering to that of a system simulated without ions.

3.4   Specific ion adsorption

3.4.1   Bulk ions

Interfaces in salt solutions give rise to a double layer of cations and anions at the surface.[64] Ions in these double layers get stuck to the surface, or adsorb, which is sometimes referred to as specific binding. Zwitterionic lipid bilayers have no net charge before ions are adsorbed, so this adsorption determines the surface charge density on the substrate. This charge is measured experimentally using the electrophoretic mobility of the vesicle. Interpretation of such experiments requires one to define a surface, often called the "slip-surface" where solvent beyond that point can be represented by a dielectric continuum. The electrostatic potential at this surface is the ζ–potential. In simulations the interface is not a simple surface, but a region without a clear point of delineation.

Hydration boundary

We identify this slip-surface boundary as the point where water orientational ordering is negligible, i.e. beyond the "slip-surface" boundary water quadrupoles are sufficiently isotropic, giving dielectric properties of water similar to that of bulk solvent. We compute this by first dividing the box into slices along the direction normal to the bilayer. For each water within a slice we compute the average value of first and second order legendre polynomial of the cosine of the angle between the box z-axis and the water O-H bond vector, and then average these values over the last 150 ns of simulated time. Figure 3.3 shows the water order parameters as a function of the distance of a slice from the bilayer center.

The first order parameter describes the in-out ordering of the bond vector with respect to the box z-axis – a vector parallel to the axis and pointing normal to the bilayer would have a positive ordering, and a vector pointing into the bilayer would have a negative ordering. We see that waters at the surface of each bilayer have a significant outward orientation at the bilayer surface, and that reverses as we move closer to the bilayer center. When compared to the system simulated without ions, we see that the monovalent ions perturb the water in-out orientation more than Mg^{2+}, especially in the case of the Mg^{2+}–Grotz *et al.*parameters.

The second order parameter roughly describes the organization of the quadrupole moments of water, and the value of this parameter can be used to compute the quadrupolar splitting values determined in deuterated water NMR experiments.[63, 89] The vertical dotted lines in figure 3.3 denote regions of interest in the bilayer based on the sign of the second order parameter. We call the innermost region of negative ordering B_{-1}, which ends when the values become positive. This next region of positive ordering is called B_+, and the following region of negative ordering is B_{-2}. Each bilayer system with ions has these regions, but they are at differing distances from the bilayer center. It should be noted that beyond the B_{-2} region the ordering does not abruptly reach zero in the systems simulated with salt.

Figure 3.3 shows monovalent ions have less organization in the B_{-1} region (inside the lipid headgroup) when compared to that of the divalent ions, whereas in regions B_+ and B_{-2} (closer
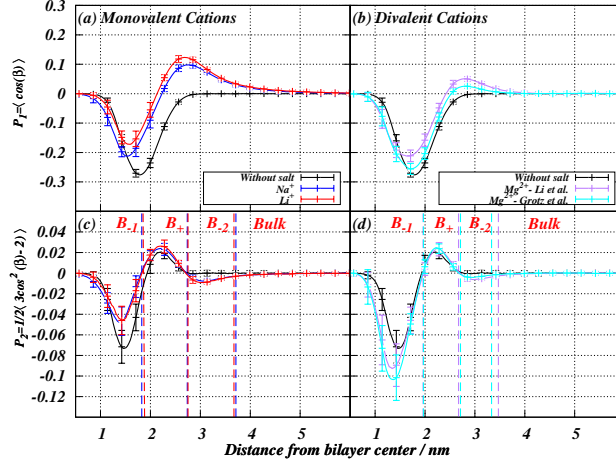
Figure 3.3: Water order parameters. The P1 and P2 calculated for monovalent cations (a,c) show greater organization in the bulk region and the B$_{-2}$ regions, and less organization within the lipid-occupied regions of the system (B$_{+}$ and B$_{-1}$) compared to the simulation without salt. On the other hand, with the presence of Mg^{2+}salts we observe an overall less pronounced effect in the bulk and B$_{-2}$ regions compared to the system without salt (b,d).

to the bilayer surface) the divalent ions show significantly less organization compared to that of monovalent salts. The hydration boundary is determined by fitting an exponential decay to the second water order parameter starting at the minimum of the B$_{-2}$ of the histogram. The decay length is used to demarcate the point where the ordering becomes zero – water beyond this region is regarded as bulk solvent. The location of the hydration boundary is noted in figure 3.3, and the distance to this point from the bilayer center is listed in table 2.5.

Poission-Boltzmann Theory

With the boundary defined, we look to the region of bulk solvent to examine the behavior of ions and ascertain that they follow the predictions of PB-theory.[64] The purpose of this endeavor is to distinguish the ions in bulk solvent from those that are adsorbed, as the density of the adsorbed ions are expected to deviate from PB-theory predictions. We must first compute all the model parameters for the number density and electrostatic potential predicted by PB-theory, and compare our simulation results to this prediction. The PB-

theory assumes that the number density of ions follow a Boltzmann distribution:

$$\rho(z) = \rho_0 \exp\left(-\bar{z}e\beta\psi(z)\right), \tag{3.4}$$

where ρ_0 is the ion density in the center of the dielectric continuum, $\bar{z}$ is the valency of the ion, $\beta = (k_b T)^{-1}$, e is the charge on an electron, and $\psi(z)$ is the electrostatic potential. The surface is defined by the hydration boundary of each system. The lengths of the solvent occupied regions, D, in each system is found by measuring the distance across the solvent from the hydration boundary of one leaflet of the bilayer to the other. These values are listed in table 3.3. This places the surfaces at $z = \pm D/2$ nm, where $z = 0$ is the center of the solvent-occupied region of the simulation box. The electrostatic potential $\psi(z)$ is modeled as a sum between two Debye-Huckle potentials:[64]

$$\psi_1(z) = \psi_s \exp\left(-K(z + \frac{D}{2})\right) \tag{3.5}$$

$$\psi_2(z) = \psi_s \exp\left(K(z - \frac{D}{2})\right) \tag{3.6}$$

$$\psi(z) = \psi_1(z) + \psi_2(z) - \left(\psi_1(0) + \psi_2(0)\right), \tag{3.7}$$

where $\psi_s = \frac{\sigma}{\epsilon_0 \epsilon} K$ is the electrostatic potential at the bilayer surface as defined by the hydration boundary, ϵ is the dielectric constant of SPC/E water $\epsilon = 70.7$,[90] and σ is the surface charge density of the bilayer leaflet.[64]

σ is determined for each system by integrating the charge density of all species within the hydration boundary on either side of the bilayer. This charge divided by the box area is the surface charge density. These values can be seen in table 3.3. Since our phospholipid is zwitterionic, all of the surface charge comes from the ions that have accumulated within the hydration boundary (see figure 3.4)
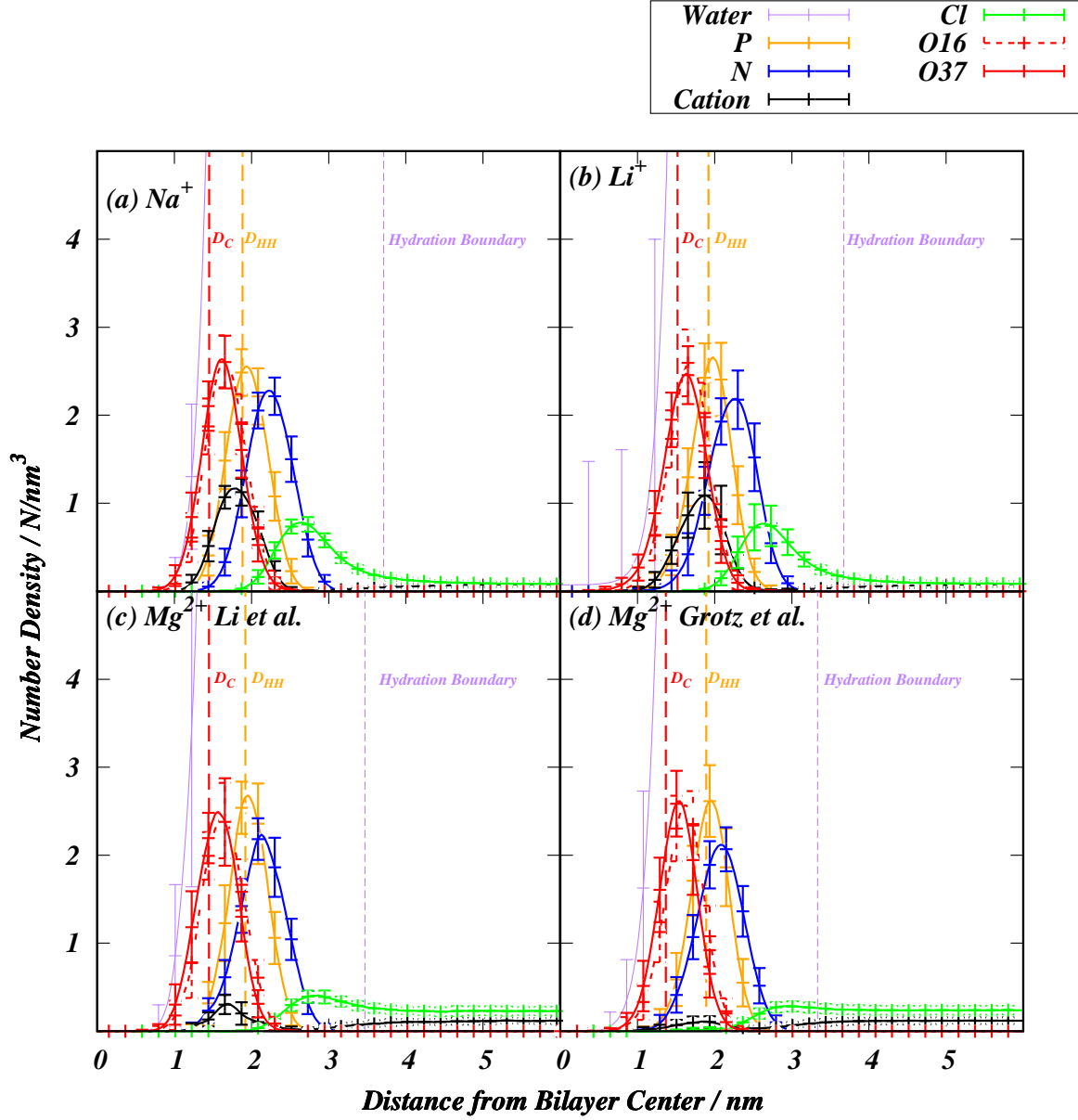
Figure 3.4: Number density of lipid headgroup species and ions near the bilayer interface. (a-b) We report that the monovalent cations show peaks near the phosphate, with accumulation of an anion peak that resembles the double layer. (c-d) Mg^{2+} does not show significant accumulation in the lipid bilayer headgroup compared to the monovalent ions, with a similarly small anion peak. However, in all systems studied, ions are accumulated near the phosphorus. Integrating the number density of cations within the hydration boundary, denoted by the purple vertical dashed line, gives the number of ions that are sterically bound. The orange vertical dashed line delineates the D_{hh} and the red vertical dashes delineate the D_C of the bilayer.

Table 3.3: Poisson-boltzmann theory parameters. These parameters are computed for each simulated system studied (excepting the bulk density ($\rho_{0,i}$), which we fit to our simulation results). These are then used to compute the number density distribution and the electrostatic potential as described by Poisson-Boltzmann theory to compare to our simulation results. σ is the surface charge density of the bilayer, D is the length of the bulk-solvent occupied region of the box, K is the Debye screening length, and $\rho_{0,i}$ is the number density of the particular ion at the center of bulk solvent.

Parameter	Na$^+$	Li$^+$	Mg^{2+}–Li et $al.$	Mg^{2+}–Grotz et $al.$
$\sigma(e/nm^2)$	0.161	0.182	0.0690	0.0476
D (nm)	26.927	26.557	26.658	25.226
K (nm^{-1})	3.331	3.333	3.913	3.921
$\rho_{0,cation}$ (nm^{-3})	0.059	0.060	0.091	0.092
$\rho_{0,anion}$ (nm^{-3})	0.062	0.063	0.183	0.185

Returning to equation 3.7, K is the inverse Debye length,

$$K = \sqrt{\sum_i \rho_{0,i} \bar{z}_i^2 \frac{e^2}{\epsilon_0 \epsilon k_b T}}, \tag{3.8}$$

where $\rho_{0,i}$ is the density of each ion in a given system at the center of bulk solvent. This is taken as an average of the number density of each ion in the solvent occupied region of the box.

Finally, we fit equation 3.4 to the density of anions in bulk solvent via ρ_0. The comparisons can be seen in figure 3.5. Past the hydration boundary of the lipid bilayer, it can be seen that the density of anions continues to climb monotonically. Additionally, the density of cations drops monotonically to a trough value before climbing closer to the bilayer center, near the phosphate groups (see figure 3.4 and 3.5).

We also compare the electrostatic potential from our simulations to the potential from PB-theory (figure 3.6). The electrostatic potential for each simulated system can be com-
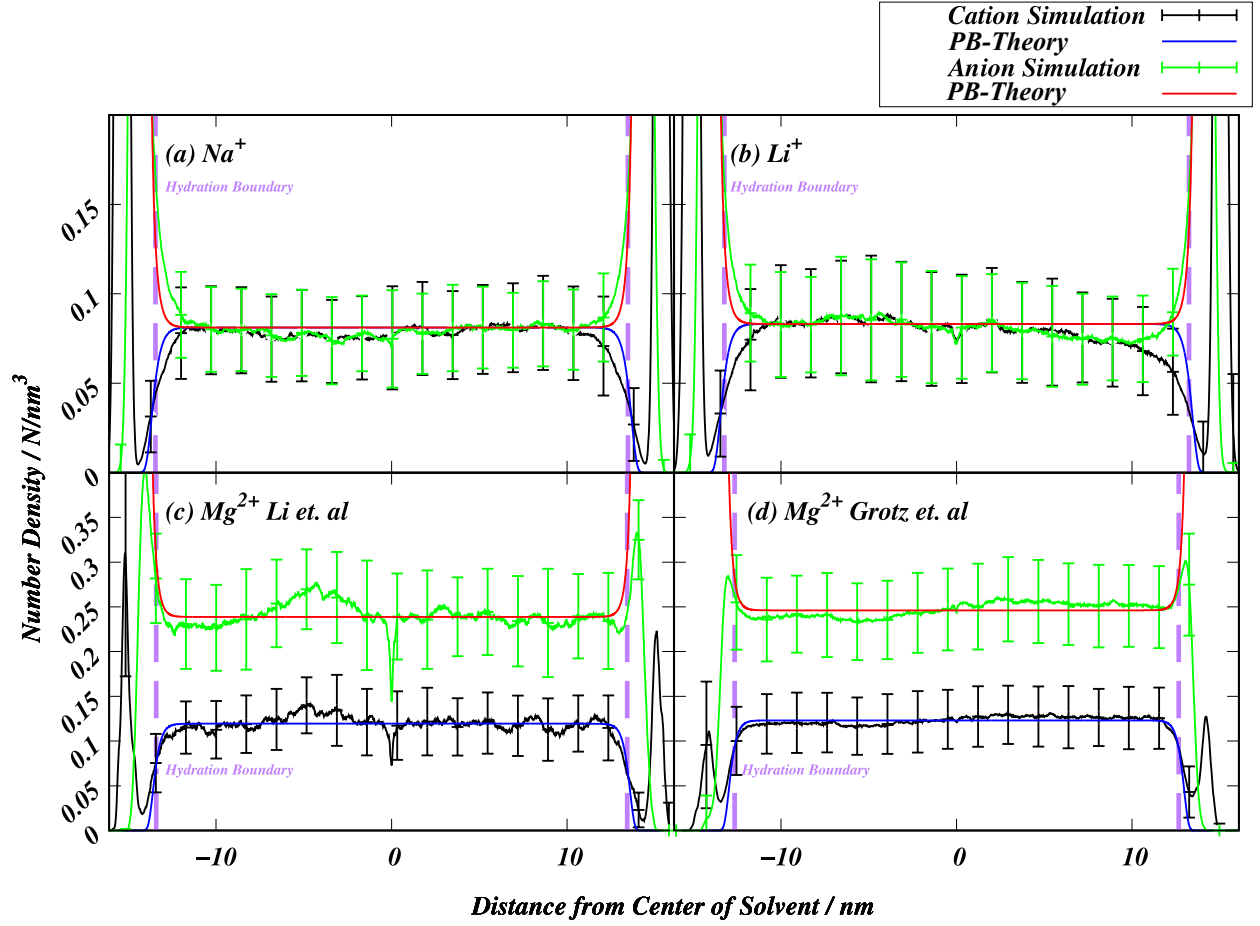
Figure 3.5: Number density of cations and anions in the bulk solvent-occupied region of each simulated system, compared with theoretical predictions from PB-theory for each calculated σ. PB-theory predictions correspond well with the simulation results within the region bounded by the hydration boundary.
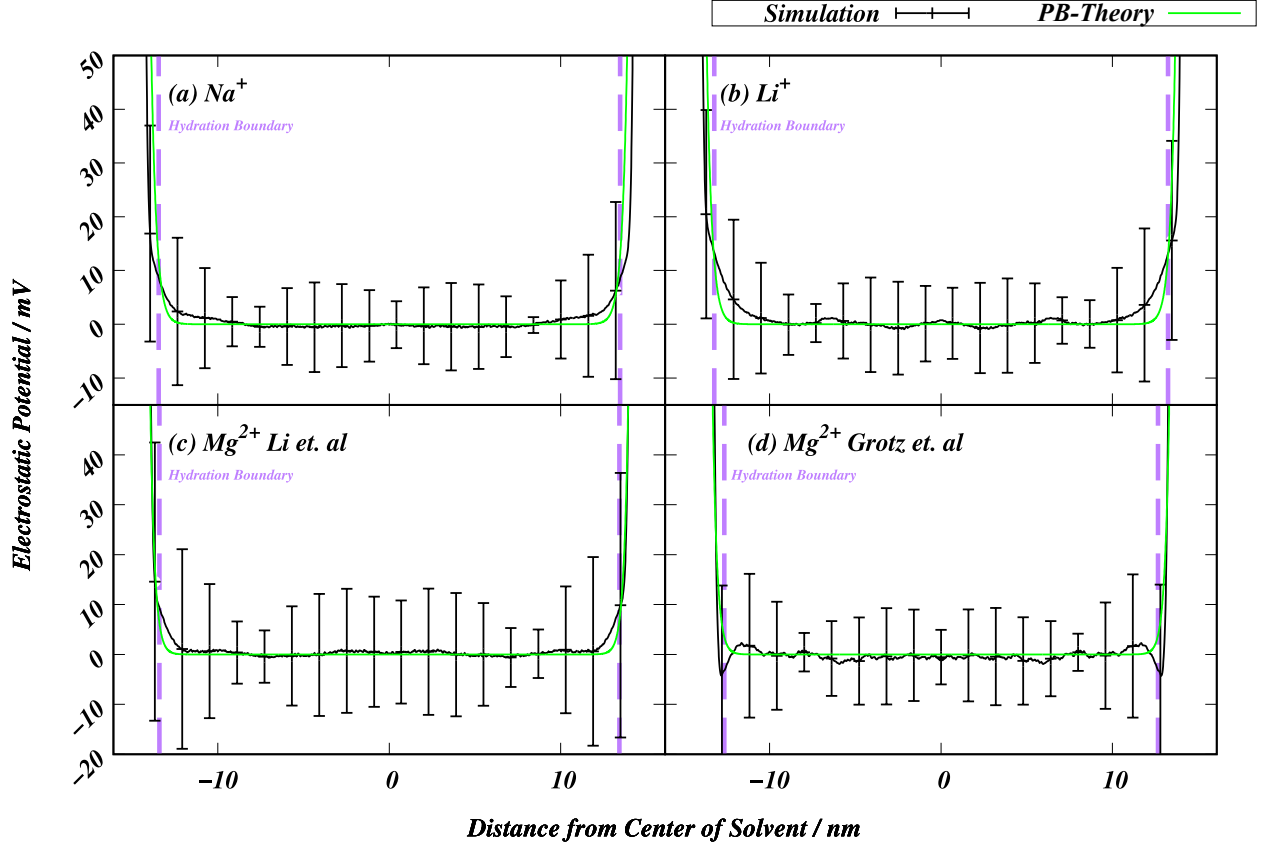
Figure 3.6: Electrostatic potential in the bulk solvent-occupied region compared to predictions from PB-theory. We report good agreement between the theoretical potential shown in green, and the simulation results shown in black, within the region bounded by the hydration bounds of the lipid bilayer.

puted by twice integrating the Poisson equation

$$\phi(z) = -\frac{1}{\epsilon_0} \int_0^z \int_0^{z'} \rho(z) dz dz' + C_1 z + C_2. \tag{3.9}$$

We set the boundary conditions that the electric field in bulk solvent must be zero, and the electrostatic potential at the box edge must be zero. The electrostatic potential from simulation agrees well with the prediction from PB-theory.

3.4.2 Adsorbed ions

The total number of adsorbed ions are counted as the number of ions within the "slip-surface" or "hydration-boundary" of the bilayer, and further characterization is based on the level of hydration of the ion. Binding constants from the Langmuir Isotherm model are often computed in experiments to describe ion binding affinity for surfaces; however, this model requires a fixed number of binding sites per lipid. The actual number of binding sites per lipid is not known. Therefore, we report the number of ions adsorbed per lipid (θ), which is related to the binding affinity of each ion for the lipid bilayer. We observe 0.51 Na^+ per lipid bound, 0.57 Li^+ per lipid, 0.13 Mg^{2+} per lipid in the Mg^{2+}–Li *et al.*system, and 0.10 Mg^{2+} per lipid in the Mg^{2+}–Grotz *et al.*system. We see a substantially larger number of Na^+ and Li^+ adsorbed per lipid than Mg^{2+}, which may be reflective of the amount of space occupied by each ion, and seems to follow the binding modes such that the more dehydrated ions correlate with a larger number of ions adsorbed per lipid. The fraction of cations adsorbed in each mode of adsorption can be seen in table 3.4, and the fractions of Cl^- anions adsorbed can be seen in supporting table S2. Cl^- adsorption fractions follow a similar trend to that of the total number of cations bound, but adsorption is almost entirely in the steric modality.

Table 3.4: Fractions per lipid of cations perfectly adsorbed, imperfectly adsorbed, sterically adsorbed, and non-adsorbed cations averaged over the last 150 ns of simulation time. These are computed by counting the number of waters in the first-coordination shell of every ion in the simulation box in every frame. For the total number of adsorbed ions, we only check if the ion is within the hydration boundary of the bilayer. We then subtract the number within this region that are completely dehydrated – these are the perfectly adsorbed ions. We further subtract any ions that have lost one or more waters – the imperfectly adsorbed ions. The remaining are considered sterically adsorbed. We also report the total number of bound ions per lipid as a measure of the affinity of the ion to the lipid bilayer – the number of Mg^{2+}ions per lipid is fall smaller than that for the more perfectly adsorbed ions $Li^+$and Na^+.

Adsorbed cations / lipid	Na^+	Li^+	Mg^{2+}–Li *et al.*	Mg^{2+}–Grotz *et al.*
Total θ	0.472	0.575	0.129	0.091
Steric θ_s	0.010	0.015	0.116	0.071
Imperfect θ_I	0.068	0.165	0.008	0.020
Perfect θ_P	0.394	0.395	0.005	0.000

Adsorption modalities

Further characterization of the adsorbed ions begins by examining the first-shell coordination partners of cations in each system. This can be counted by first determining a cutoff value for the first hydration shell of each ion – the values for this cutoff are 3.2 Å for Na^+, 2.7 Å for Li^+, 3.3 Å for Mg^{2+}, and 3.0 Å for Cl^-. These values are determined from radial distribution functions for water oxygen (or water hydrogen in the case of Cl^-) around each. This cutoff is used to produce a neighborlist for ions across each simulation in every frame, and count the number of neighbors within this cutoff. These data are histogrammed and averaged over the last 150ns of simulation time. The results for this are presented in figure 3.7.

The number of perfectly adsorbed ions is determined by counting the number of ions without any remaining waters in their first coordination shell. It is observed that in the Na^+system, a majority of the ions adsorbed to the bilayer are completely dehydrated. The
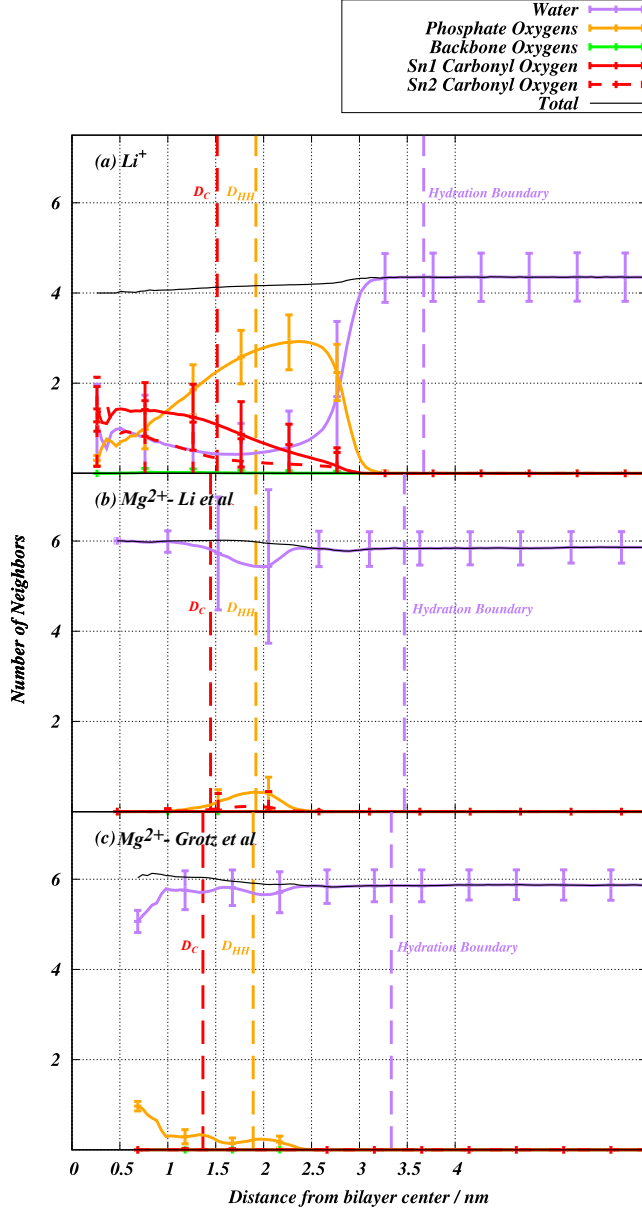
Figure 3.7: First shell coordination partners for Li$^+$ and Mg^{2+} in each simulation. These are computed over the last 150ns of simulation time in each system by counting the atoms of each species within a cutoff of each ion in the system, and histogramming the data based on the position of the ion. The dotted vertical lines denote the various bilayer surfaces – the vertical black line delineates the hydration boundary of the bilayer, the vertical blue line delineates the D_{HH}, and the vertical red line delineates the D_C. Li$^+$(a) retains some water coordination well into the bilayer interface. Mg^{2+}–Li *et al.*(b) on the other hand does not lose nearly any first-shell coordinating waters in the bilayer, with some exchange for phosphate oxygens. The Mg^{2+}–Grotz *et al.*(c) parameters yield again more exchange but relatively far less than the monovalent ions.

Li$^+$system has a similar fraction of perfectly adsorbed ions compared to Na$^+$, and practically no perfectly adsorbed ions are seen in any of the Mg^{2+}simulations. Cl$^-$anions are not seen adsorbed perfectly in any simulation.

Similarly to the perfect adsorption case, imperfectly adsorbed ions are counted as ions with one or more waters in their first coordination shell, but missing at least one water from the shell. We use the number of coordinating waters of an ion in the bulk solvent region of our simulation as the maximum coordination number for the ion (Figure 7). This gives a coordination number of 4 for Li$^+$and 6 for Mg^{2+}. We calculate the number of imperfectly adsorbed ions by counting the number of ions with one or more water missing from their hydration shell, and then subtracting the number of perfectly adsorbed ions. We see more than twice the fraction of these ions in the Li$^+$system compared to the Na$^+$system. Mg^{2+}shows an insignificant number of imperfectly adsorbed ions. Cl$^-$adsorbs in a large fraction imperfectly, as they begin to interact with the headgroup trimethylammonium.

The remaining ions are considered sterically adsorbed – this number is whatever ions remain after subtracting the perfect and imperfectly adsorbed ions from the number of overall adsorbed ions based on the position of the hydration boundary. Mg^{2+}seems to have most of the ions in this adsorption mode, where Na$^+$and Li$^+$do not adsorb in this way in significant numbers. Additionally, Cl$^-$shows significant steric adsorption.

These data raise the question, what determines the mode of adsorption for a given ion? Since everything else, such as the substrate and the solvent, are held constant, the magnitude of the electric field at the position of the hydration shell of each ion is all that remains to determine the adsorption modality of the ion (figure **??**). The electric field strength of each ion is calculated by applying Coulomb's law to a point charge, placing the test charge at the position of the first hydration shell of the ion in question. We note that the Mg^{2+}–Li *et al.*ion keeps waters slightly closer in the hydration shell compared to the Mg^{2+}–Grotz *et al.*model,resulting in a stronger electric field produced at this point by that ion. The largest ion with the smallest charge-density Na$^+$dehydrates completely in the largest fraction.
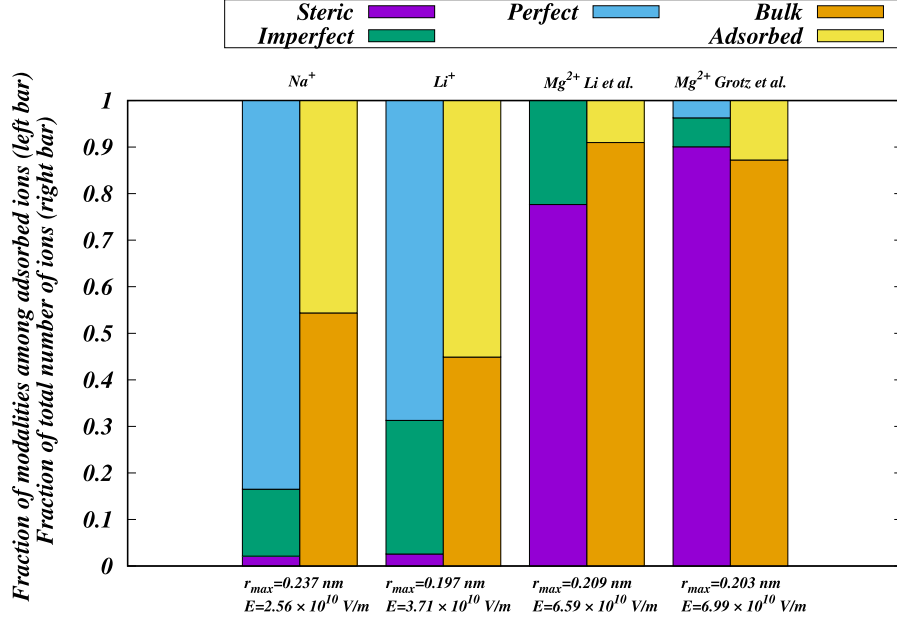
Figure 3.8: Fractions of ion-adsorption modality per each simulated system as a function of electric field strength. Here we show that the fractions of ions adsorbed in each modality follow a trend with an increasing electric field strength at the hydration shell of the cation. The overall trend is that the cations with the weakest field at the hydration shell position adsorb more perfectly, and as the field strength increases more ions adsorb imperfectly and then sterically. We note that little correlation with field strength can be seen in the total number adsorbed per ion.

Li$^+$is smaller, and thus the field near the first shell is stronger and can hold waters a little better than Na$^+$. Mg^{2+}is similar in size to Li$^+$, but has a 2+ charge and holds onto waters substantially more than either of the monovalent ions. We also note that the $\left\|\vec{E}\right\|$ does not exhibit strong correlation with the fraction of the total number of ions adsorbed in each system, it only determines the adsorption mode.

3.5 Conclusions

Ion adsorption to porous interfaces is a complex interplay between solvent–surface, solvent–ion, and solvent–solvent interactions. With the solvent–surface and solvent–solvent interactions held constant, we identify three different adsorption modalities of ions based on the degree of dehydration of the ion upon adsorption. The binding modality of a particular ion is significantly correlated with the electric field strength of the ion at the position of the first hydration shell, with stronger fields encouraging less dehydration of the ion upon adsorption to the surface (figure 8). This affect appears irrespective of the force-field used in the case of Mg^{2+}, which primarily adsorbs in the non-Langmuir type steric modality.

Furthermore, we identify several bilayer structural parameters that can be verified experimentally via x-ray scattering, neutron scattering, or various NMR methods (figures 1, 2, and 3 respectively). While the effect on lipid bilayer structure is not obvious in the electron density (figure 1), the pertubation can be seen in the D$_{\mathrm{B}}$ and water density – the less hydrated ions induce slight thickening of the lipid bilayer. This is reinforced by the chain ordering, where these ions increase chain ordering (figure 2) while the hydrated ions leave the lipid bilayer structure similar to that of the no-salt case. These two results can be verified experimentally via solvent deuterium NMR, and lipid chain NMR. In the case of POPC, we expect deuterium solvent quadrupolar splitting values will be larger for the less hydrated ions Na$^+$and Li$^+$when compared to the more hydrated Mg^{2+} (figure 3). We also expect the lipid chain order parameters to follow the opposite trend, with the monovalent ions inducing more ordering and Mg^{2+}inducing a smaller change from the no-salt system. We also expect that the adsorption of Mg^{2+}will be less detectable via the electrophoretic mobility of a vesicle

in an MgCl salt solution, as the energy required to remove a hydrated ion from beneath the slip-surface of a vesicle may be low enough to allow their escape, while a dehydrated ion may remain adsorbed. These experiments are needed to verify these conclusions.

4 Alteration of lipid bilayer structure by adsorbed ions

5   Conclusions

IDK Man I don't know what to say here! I guess I should read all of that one more time before I write this part...

References

[1] M. L. Berkowitz, Biomembrane Simulations: Computational Studies of Biological Membranes, CRC Press, 2019.

[2] S. A. Pandit, H. L. Scott, Simulations and models of lipid bilayers, in: Soft Matter: Lipid Bilayers and Red Blood Cells, Vol. 4, Wiley Online Library, 2008, Ch. 1, pp. 1–82.

[3] J. Kruczek, S.-W. Chiu, E. Jakobsson, S. A. Pandit, Effects of lithium and other monovalent ions on palmitoyl oleoyl phosphatidylcholine bilayer, Langmuir 33 (4) (2017) 1105–1115.
URL http://dx.doi.org/10.1021/acs.langmuir.6b04166

[4] J. Kruczek, S.-W. Chiu, S. Varma, E. Jakobsson, S. A. Pandit, Interactions of monovalent and divalent cations at palmitoyl-oleoyl-phosphatidylcholine interface, Langmuir 35 (32) (2019) 10522–10532.

[5] M. Saunders, M. Steele, W. Lavigne, S. Varma, S. A. Pandit, Interaction of salt with ether-and ester-linked phospholipid bilayers, Biochimica et Biophysica Acta (BBA)-Biomembranes 1861 (5) (2019) 907–915.

[6] R. A. Böckmann, A. Hac, T. Heimburg, H. Grubmüller, Effect of sodium chloride on a lipid bilayer, Biophysical Journal 85 (3) (2003) 1647–1655.

[7] A. Cordomi, O. Edholm, J. J. Perez, Effect of ions on a dipalmitoyl phosphatidylcholine bilayer. a molecular dynamics simulation study, The Journal of Physical Chemistry B 112 (5) (2008) 1397–1408.

[8] A. A. Gurtovenko, I. Vattulainen, Effect of nacl and kcl on phosphatidylcholine and phosphatidylethanolamine lipid membranes: insight from atomic-scale simulations for understanding salt-induced effects in the plasma membrane, The Journal of Physical Chemistry B 112 (7) (2008) 1953–1962.

[9] A. Cordomi, O. Edholm, J. J. Perez, Effect of force field parameters on sodium and potassium ion binding to dipalmitoyl phosphatidylcholine bilayers, Journal of chemical theory and computation 5 (8) (2009) 2125–2134.

[10] P. Jurkiewicz, L. Cwiklik, A. Vojtíšková, P. Jungwirth, M. Hof, Structure, dynamics, and hydration of popc/pops bilayers suspended in nacl, kcl, and cscl solutions, Biochimica et Biophysica Acta (BBA)-Biomembranes 1818 (3) (2012) 609–616.

[11] G. Pabst, A. Hodzic, J. Štrancar, S. Danner, M. Rappolt, P. Laggner, Rigidification of neutral lipid bilayers in the presence of salts, Biophysical journal 93 (8) (2007) 2688–2696.

[12] H. I. Petrache, S. Tristram-Nagle, D. Harries, N. Kučerka, J. F. Nagle, V. A. Parsegian, Swelling of phospholipids by monovalent salt, Journal of lipid research 47 (2) (2006) 302–309.

[13] D. Uhríková, N. Kučerka, J. Teixeira, V. Gordeliy, P. Balgavỳ, Structural changes in dipalmitoylphosphatidylcholine bilayer promoted by ca2+ ions: a small-angle neutron scattering study, Chemistry and physics of lipids 155 (2) (2008) 80–89.

[14] I. S. Joung, T. E. Cheatham III, Determination of alkali and halide monovalent ion parameters for use in explicitly solvated biomolecular simulations, The journal of physical chemistry B 112 (30) (2008) 9020–9041.

[15] S.-W. Chiu, S. A. Pandit, H. Scott, E. Jakobsson, An improved united atom force field for simulation of mixed lipid bilayers, The Journal of Physical Chemistry B 113 (9) (2009) 2748–2763.

[16] S. Varma, S. B. Rempe, Multibody effects in ion binding and selectivity, Biophysical journal 99 (10) (2010) 3394–3401.

[17] V. Wineman-Fisher, Y. Al-Hamdani, I. Addou, A. Tkatchenko, S. Varma, Ion-hydroxyl interactions: From high-level quantum benchmarks to transferable polarizable force fields, Journal of chemical theory and computation 15 (4) (2019) 2444–2453.

[18] R. Vácha, P. Jurkiewicz, M. Petrov, M. L. Berkowitz, R. A. Bockmann, J. Barucha-Kraszewska, M. Hof, P. Jungwirth, Mechanism of interaction of monovalent ions with phosphatidylcholine lipid membranes, The Journal of Physical Chemistry B 114 (29) (2010) 9504–9509.

[19] I. Vorobyov, T. W. Allen, The electrostatics of solvent and membrane interfaces and the role of electronic polarizability, The Journal of Chemical Physics 132 (18) (2010) 05B602.

[20] J. Melcr, H. Martinez-Seara, R. Nencini, J. Kolafa, P. Jungwirth, O. S. Ollila, Accurate binding of sodium and calcium to a popc bilayer by effective inclusion of electronic polarization, The Journal of Physical Chemistry B 122 (16) (2018) 4546–4557.

[21] P. Chen, I. Vorobyov, B. Roux, T. W. Allen, Molecular dynamics simulations based on polarizable models show that ion permeation interconverts between different mechanisms as a function of membrane thickness, The Journal of Physical Chemistry B 125 (4) (2021) 1020–1035.

[22] G. Lee Warren, J. E. Davis, S. Patel, Origin and control of superlinear polarizability scaling in chemical potential equalization methods, The Journal of chemical physics 128 (14) (2008) 144110.

[23] D. Boda, D. Henderson, The effects of deviations from lorentz–berthelot rules on the properties of a simple mixture, Molecular Physics 106 (20) (2008) 2367–2370.

[24] C. M. Baker, P. E. Lopes, X. Zhu, B. Roux, A. D. MacKerell Jr, Accurate calculation of hydration free energies using pair-specific lennard-jones parameters in the charmm drude polarizable force field, Journal of chemical theory and computation 6 (4) (2010) 1181–1198.

[25] J. Yoo, A. Aksimentiev, Improved parametrization of li+, na+, k+, and mg2+ ions for all-atom molecular dynamics simulations of nucleic acid systems, The journal of physical chemistry letters 3 (1) (2012) 45–50.

[26] M. Fyta, R. R. Netz, Ionic force field optimization based on single-ion and ion-pair solvation properties: Going beyond standard mixing rules, The Journal of chemical physics 136 (12) (2012) 124103.

[27] S. Mamatkulov, M. Fyta, R. R. Netz, Force fields for divalent cations based on single-ion and ion-pair properties, The Journal of chemical physics 138 (2) (2013) 024505.

[28] R. M. Venable, Y. Luo, K. Gawrisch, B. Roux, R. W. Pastor, Simulations of anionic lipid membranes: development of interaction-specific ion parameters and validation using nmr data, The journal of physical chemistry B 117 (35) (2013) 10183–10192.

[29] A. Savelyev, A. D. MacKerell Jr, Balancing the interactions of ions, water, and dna in the drude polarizable force field, The Journal of Physical Chemistry B 118 (24) (2014) 6742–6757.

[30] H. Li, V. Ngo, M. C. Da Silva, D. R. Salahub, K. Callahan, B. Roux, S. Y. Noskov, Representation of ion–protein interactions using the drude polarizable force-field, The Journal of Physical Chemistry B 119 (29) (2015) 9401–9416.

[31] A. Savelyev, A. D. MacKerell Jr, Competition among li+, na+, k+, and rb+ monovalent ions for dna in molecular dynamics simulations using the additive charmm36 and drude polarizable force fields, The Journal of Physical Chemistry B 119 (12) (2015) 4428–4440.

[32] Z. Jing, R. Qi, C. Liu, P. Ren, Study of interactions between metal ions and protein model compounds by energy decomposition analyses and the amoeba force field, The Journal of chemical physics 147 (16) (2017) 161733.

[33] M. M. Reif, C. Kallies, V. Knecht, Effect of sodium and chloride binding on a lecithin bilayer. a molecular dynamics study, Membranes 7 (1) (2017) 5.

[34] J. C. Fogarty, S.-W. Chiu, P. Kirby, E. Jakobsson, S. A. Pandit, Automated optimization of water–water interaction parameters for a coarse-grained model, The Journal of Physical Chemistry B 118 (6) (2014) 1603–1611.

[35] J. C. Fogarty, High Dimensional Non-Linear Optimization of Molecular Models, University of South Florida, 2014.

[36] S. Varma, S. B. Rempe, Coordination numbers of alkali metal ions in aqueous solutions, Biophysical chemistry 124 (3) (2006) 192–199.

[37] P. Mason, S. Ansell, G. Neilson, Neutron diffraction studies of electrolytes in null water: a direct determination of the first hydration zone of ions, Journal of Physics: Condensed Matter 18 (37) (2006) 8437.

[38] M. Galib, M. Baer, L. Skinner, C. Mundy, T. Huthwelker, G. Schenter, C. Benmore, N. Govind, J. L. Fulton, Revisiting the hydration structure of aqueous na+, The Journal of chemical physics 146 (8) (2017) 084504.

[39] J. Timko, D. Bucher, S. Kuyucak, Dissociation of nacl in water from ab initio molecular dynamics simulations, The Journal of chemical physics 132 (11) (2010) 114510.

[40] P. Smirnov, Structure of the nearest environment of na+, k+, rb+, and cs+ ions in oxygen-containing solvents, Russian Journal of General Chemistry 90 (9) (2020) 1693–1702.

[41] V. Blum, R. Gehrke, F. Hanke, P. Havu, V. Havu, X. Ren, K. Reuter, M. Scheffler, Ab initio molecular simulations with numeric atom-centered orbitals, Computer Physics Communications 180 (11) (2009) 2175–2196.

[42] J. P. Perdew, K. Burke, M. Ernzerhof, Generalized gradient approximation made simple, Physical review letters 77 (18) (1996) 3865.

[43] C. Adamo, V. Barone, Toward reliable density functional methods without adjustable parameters: The pbe0 model, The Journal of chemical physics 110 (13) (1999) 6158–6170.

[44] A. Tkatchenko, M. Scheffler, Accurate molecular van der waals interactions from ground-state electron density and free-atom reference data, Physical review letters 102 (7) (2009) 073005.

[45] V. Wineman-Fisher, J. M. Delgado, P. R. Nagy, E. Jakobsson, S. A. Pandit, S. Varma, Transferable interactions of li+ and mg2+ ions in polarizable models, The Journal of Chemical Physics 153 (10) (2020) 104113.

[46] V. Wineman-Fisher, Y. Al-Hamdani, P. R. Nagy, A. Tkatchenko, S. Varma, Improved description of ligand polarization enhances transferability of ion–ligand interactions, The Journal of Chemical Physics 153 (9) (2020) 094115.

[47] M. J. Abraham, T. Murtola, R. Schulz, S. Páll, J. C. Smith, B. Hess, E. Lindahl, Gromacs: High performance molecular simulations through multi-level parallelism from laptops to supercomputers, SoftwareX 1 (2015) 19–25.

[48] S. Pall, M. J. Abraham, C. Kutzner, B. Hess, E. Lindahl, Tackling exascale software challenges in molecular dynamics simulations with gromacs, in: International Conference on Exascale Applications and Software, Springer, 2014, pp. 3–27.

[49] D. V. D. Spoel, E. Lindahl, B. Hess, G. Groenhof, A. Mark, H. Berendsen, Gromacs: fast, flexible, free, J. Comput. Chem. 26 (2005) 1701.

[50] E. Lindahl, B. Hess, D. Van Der Spoel, Gromacs 3.0: a package for molecular simulation and trajectory analysis, Molecular modeling annual 7 (8) (2001) 306–317.

[51] H. J. Berendsen, D. van der Spoel, R. van Drunen, Gromacs: a message-passing parallel molecular dynamics implementation, Computer Physics Communications 91 (1-3) (1995) 43–56.

[52] H. Berendsen, J. Grigera, T. Straatsma, The missing term in effective pair potentials, Journal of Physical Chemistry 91 (24) (1987) 6269–6271.

[53] S. Nosé, M. Klein, Constant pressure molecular dynamics for molecular systems, Molecular Physics 50 (5) (1983) 1055–1076.

[54] M. Parrinello, A. Rahman, Polymorphic transitions in single crystals: A new molecular dynamics method, Journal of Applied physics 52 (12) (1981) 7182–7190.

[55] B. Hess, H. Bekker, H. J. C. Berendsen, J. G. E. M. Fraaije, Lincs: A linear constraint solver for molecular simulations, Journal of Computational Chemistry 18 (12) (1997) 1463–1472.
URL http://dx.doi.org/10.1002/(SICI)1096-987X(199709)18:12<1463::AID-JCC4>3.0.CO;2-H

[56] U. Essmann, L. Perera, M. L. Berkowitz, T. Darden, H. Lee, L. G. Pedersen, A smooth particle mesh ewald method, The Journal of chemical physics 103 (19) (1995) 8577–8593.

[57] H. I. Petrache, S. E. Feller, J. F. Nagle, Determination of component volumes of lipid bilayers from sin Biophysical Journal 72 (5) (1997) 2237–2242.
URL http://www.ncbi.nlm.nih.gov/pmc/articles/PMC1184418/

[58] J. F. Nagle, S. Tristram-Nagle, Structure of lipid bilayers, Biochimica et Biophysica Acta (BBA)-Reviews on Biomembranes 1469 (3) (2000) 159–195.

[59] J. C. Fogarty, M. Arjunwadkar, S. A. Pandit, J. Pan, Atomically detailed lipid bilayer models for the interpretation of small angle neutron and x-ray scattering data, Biochimica et Biophysica Acta (BBA)-Biomembranes 1848 (2) (2015) 662–672.

[60] E. Egberts, H. Berendsen, Molecular dynamics simulation of a smectic liquid crystal with atomic detail, The Journal of chemical physics 89 (6) (1988) 3718–3732.

[61] J.-P. Douliez, A. Leonard, E. J. Dufourc, Restatement of order parameters in biomembranes: calculation of cc bond order parameters from cd quadrupolar splittings., Biophysical journal 68 (5) (1995) 1727.

[62] S. Varma, S. B. Rempe, Structural transitions in ion coordination driven by changes in competition for ligand binding, Journal of the American Chemical Society 130 (46) (2008) 15405–15419.

[63] K. Åman, E. Lindahl, O. Edholm, P. Håkansson, P.-O. Westlund, Structure and dynamics of interfacial water in an l α phase lipid bilayer from molecular dynamics simulations, Biophysical journal 84 (1) (2003) 102–115.

[64] J. N. Israelachvili, Intermolecular and surface forces, Academic press, 2011.

[65] O. Stern, The theory of the electrolytic double-layer, Z. Elektrochem 30 (508) (1924) 1014–1020.

[66] D. C. Grahame, The electrical double layer and the theory of electrocapillarity., Chemical reviews 41 (3) (1947) 441–501.

[67] M. C. Smith, R. M. Crist, J. D. Clogston, S. E. McNeil, Zeta potential: a case study of cationic, anionic, and neutral liposomes, Analytical and bioanalytical chemistry 409 (2017) 5779–5787.

[68] J. Marra, J. Israelachvili, Direct measurements of forces between phosphatidylcholine and phosphatidylethanolamine bilayers in aqueous electrolyte solutions, Biochemistry 24 (17) (1985) 4608–4618.

[69] J. Pan, F. A. Heberle, S. Tristram-Nagle, M. Szymanski, M. Koepfinger, J. Katsaras, N. Kucerka, Molecular structures of fluid phase phosphatidylglycerol bilayers as determined by small angle neutron and x-ray scattering, Biochimica et Biophysica Acta (BBA)-Biomembranes 1818 (9) (2012) 2135–2148.

[70] J. Pan, X. Cheng, F. A. Heberle, B. Mostofian, N. Kucerka, P. Drazba, J. Katsaras, Interactions between ether phospholipids and cholesterol as determined by scattering and molecular dynamics simulations, The Journal of Physical Chemistry B 116 (51) (2012) 14829–14838.

[71] H. Casal, H. Mantsch, H. Hauser, Infrared and 31p-nmr studies of the interaction of mg2+ with phosphatidylserines: effect of hydrocarbon chain unsaturation, Biochimica et Biophysica Acta (BBA)-Biomembranes 982 (2) (1989) 228–236.

[72] S. A. Pandit, D. Bostick, M. L. Berkowitz, Molecular dynamics simulation of a dipalmitoylphosphatidylcholine bilayer with nacl, Biophysical journal 84 (6) (2003) 3743–3750.

[73] M. L. Berkowitz, D. L. Bostick, S. Pandit, Aqueous solutions next to phospholipid membrane surfaces: insights from simulations, Chemical reviews 106 (4) (2006) 1527–1539.

[74] V. Kalinin, C. Radke, An ion-binding model for ionic surfactant adsorption at aqueous-fluid interfaces, Colloids and Surfaces A: Physicochemical and Engineering Aspects 114 (1996) 337–350.

[75] M. Saunders, V. Wineman-Fisher, E. Jakobsson, S. Varma, S. A. Pandit, High-dimensional parameter search method to determine force field mixing terms in molecular simulations, Langmuir 38 (9) (2022) 2840–2851.

[76] J. C. Bowman, T. K. Lenz, N. V. Hud, L. D. Williams, et al., Cations in charge: magnesium ions in rna folding and catalysis, Current opinion in structural biology 22 (3) (2012) 262.

[77] L. Rulíšek, J. Šponer, Outer-shell and inner-shell coordination of phosphate group to hydrated metal ions (mg2+, cu2+, zn2+, cd2+) in the presence and absence of nucleobase. the role of nonelectrostatic effects, The Journal of Physical Chemistry B 107 (8) (2003) 1913–1923.

[78] T. Dudev, Lin, M. Dudev, C. Lim, First- second shell interactions in metal binding sites in proteins: A pdb survey and dft/cdm calculations, Journal of the American Chemical Society 125 (10) (2003) 3168–3180.

[79] D. Pörschke, The mode of mg++ binding to oligonucleotides. inner sphere complexes as markers for recognition?, Nucleic Acids Research 6 (3) (1979) 883–898.

[80] A. S. Petrov, J. Funseth-Smotzer, G. R. Pack, Computational study of dimethyl phosphate anion and its complexes with water, magnesium, and calcium, International journal of quantum chemistry 102 (5) (2005) 645–655.

[81] P. Li, B. P. Roberts, D. K. Chakravorty, K. M. Merz Jr, Rational design of particle mesh ewald compatible lennard-jones parameters for+ 2 metal cations in explicit solvent, Journal of chemical theory and computation 9 (6) (2013) 2733–2748.

[82] K. K. Grotz, N. Schwierz, Optimized magnesium force field parameters for biomolecular simulations with accurate solvation, ion-binding, and water-exchange properties in spc/e, tip3p-fb, tip4p/2005, tip4p-ew, and tip4p-d, Journal of Chemical Theory and Computation 18 (1) (2021) 526–537.

[83] K. K. Grotz, S. Cruz-León, N. Schwierz, Optimized magnesium force field parameters for biomolecular simulations with accurate solvation, ion-binding, and water-exchange properties, Journal of Chemical Theory and Computation 17 (4) (2021) 2530–2540.

[84] M. Abraham, D. van der Spoel, E. Lindahl, B. Hess, the gromacs development team gromacs user manual version 5.1. 2; 2016, MJ Abraham, T. Murtola, R. Schulz, S. Páll, JC Smith, B. Hess, E. Lindahl, SoftwareX 1 (2015) 19.

[85] N. Michaud-Agrawal, E. J. Denning, T. B. Woolf, O. Beckstein, Mdanalysis: a toolkit for the analysis of molecular dynamics simulations, Journal of computational chemistry 32 (10) (2011) 2319–2327.

[86] R. J. Gowers, M. Linke, J. Barnoud, T. J. E. Reddy, M. N. Melo, S. L. Seyler, J. Domanski, D. L. Dotson, S. Buchoux, I. M. Kenney, et al., Mdanalysis: a python package for the rapid analysis of molecular dynamics simulations, Tech. rep., Los Alamos National lab.(LANL), Los Alamos, NM (United States) (2019).

[87] O. Allnér, L. Nilsson, A. Villa, Magnesium ion–water coordination and exchange in biomolecular simulations, Journal of chemical theory and computation 8 (4) (2012) 1493–1502.

[88] J. M. Delgado, P. R. Nagy, S. Varma, Polarizable amoeba model for simulating mg2+· protein· nucleotide complexes, Journal of Chemical Information and Modeling 64 (2) (2023) 378–392.

[89] J. Kruczek, M. Saunders, M. Khosla, Y. Tu, S. A. Pandit, Molecular dynamics simulations of ether-and ester-linked phospholipids, Biochimica et Biophysica Acta (BBA)-Biomembranes 1859 (12) (2017) 2297–2307.

[90] M. R. Reddy, M. Berkowitz, The dielectric constant of spc/e water, Chemical physics letters 155 (2) (1989) 173–176.